

# The $s$ process in asymptotic giant branch stars of low metallicity and the composition of carbon-enhanced metal-poor stars

Maria Lugaro

*Monash Centre for Astrophysics (MoCA), Monash University, Clayton VIC 3800, Australia*

Maria.Lugaro@monash.edu

Amanda I. Karakas

*Research School of Astronomy & Astrophysics, Mount Stromlo Observatory, Weston Creek  
ACT 2611, Australia*

akarakas@mso.anu.edu.au

Richard J. Stancliffe

*Monash Centre for Astrophysics (MoCA), Monash University, Clayton VIC 3800, Australia*

*Research School of Astronomy & Astrophysics, Mount Stromlo Observatory, Weston Creek  
ACT 2611, Australia*

rjs@mso.anu.edu.au

and

Carlos Rijs

*Monash Centre for Astrophysics (MoCA), Monash University, Clayton VIC 3800, Australia*

cjrij1@student.monash.edu

## ABSTRACT

We present models for the *slow* neutron-capture process ( $s$  process) in asymptotic giant branch (AGB) stars of metallicity  $[\text{Fe}/\text{H}] = -2.3$  and masses  $0.9 M_{\odot}$  to  $6 M_{\odot}$ . We encountered different regimes of neutron-capture nucleosynthesis increasing in importance as the stellar mass decreases: the  $^{22}\text{Ne}(\alpha, n)^{25}\text{Mg}$  reaction activated during the thermal pulses, the  $^{13}\text{C}(\alpha, n)^{16}\text{O}$  reaction activated in

---

<sup>1</sup>Monash Centre for Astrophysics (MoCA), Monash University, Clayton VIC 3800, Australia

radiative conditions during the interpulse periods, and the  $^{13}\text{C}(\alpha, n)^{16}\text{O}$  reaction activated during the thermal pulses, also as a result of mild proton ingestion episodes. The models where the  $^{13}\text{C}$  burns radiatively (masses  $\simeq 2 M_{\odot}$ ) produce an overall good match to carbon-enhanced metal-poor (CEMP) stars showing *s*-process enhancements (CEMP-*s*), except they produce too much Na and F. On the other hand, none of our models can provide a match to the composition of CEMP stars also showing *rapid*-process enhancements (CEMP-*s/r*). The models fail to reproduce the observed Eu abundances, and they also fail to reproduce the correlation between the Eu and Ba abundances. They also cannot match the ratio of heavy to light *s*-process elements observed in many CEMP-*s/r* stars, which can be more than ten times higher than in the solar system. To explain the composition of CEMP-*s/r* stars we need to invoke the existence of a different “*s/r*” neutron-capture process either with features in-between the *s* and the *r* processes, or generated by superpositions of different neutron-capture processes in the same astrophysical site or in sites linked to each other - for example, in multiple stellar systems.

*Subject headings:* Nucleosynthesis, Abundances, Stars: Abundances, Stars: AGB and Post-AGB

## 1. Introduction

Following on from the discovery of a large number of halo stars with peculiar chemical compositions the last decade has seen much interest sparked in detailed spectroscopic observations and nucleosynthetic models of stars of low metallicity (Beers & Christlieb 2005; Sneden et al. 2008). These peculiar compositions provide important constraints on the evolution and nucleosynthesis of the low-metallicity stars that existed in the early Galaxy. By interpreting the observations in the light of stellar nucleosynthesis models we can derive clues as to the sites and nature of the first nucleosynthetic processes in the Galaxy. This may ultimately provide important insights into the form of the initial mass function of the first stars. The composition of metal-poor stars may also provide constraints on cold dark matter cosmological models of the formation of galaxies, which predict that galactic halos may be composed of different components of possibly different composition (e.g., Carollo et al. 2007).

Roughly 10-20% (Cohen et al. 2005; Lucatello et al. 2006; Carollo et al. 2011) of old halo

stars are enriched in carbon ( $[C/Fe]^1 > 1$ ) and are referred to as carbon-enhanced metal-poor (CEMP) stars. Most CEMP stars are also enriched in nitrogen, with  $[N/Fe] > 1$ . In most cases  $[N/Fe] < [C/Fe]$ , but also  $[N/Fe] \sim [C/Fe]$  and  $[N/Fe] > [C/Fe]$  are found in roughly 10% and 5%, respectively, of the total number of CEMP stars. Roughly 2/3 of CEMP stars also show enrichments in the elements heavier than iron, which are produced by neutron-capture processes (Aoki et al. 2007; Sneden et al. 2008). These enhancements range from pure  $s$  enhancements, of elements made primarily via *slow*-neutron captures (the  $s$  process) in the case of “CEMP- $s$ ” stars ( $[Ba/Fe] > 1$ ), to  $s$  and  $r$  enhancements, of elements made via the  $s$  process and the  $r$  process, i.e., *rapid* neutron captures (the  $r$  process) in the case of “CEMP- $s/r$ ” stars with  $[Eu/Fe] > 1$  and  $[Ba/Eu] > 0$  (Jonsell et al. 2006). There are also halo stars with pure  $r$  enhancements, so-called  $rI$  (usually classified by setting  $0.5 < [Eu/Fe] < 1$ ) and  $rII$  ( $[Eu/Fe] > 1$ ), one of which, the famous CS 22892-052 (Sneden et al. 2003), belongs to the CEMP star family. CEMP stars without enhancements in the elements heavier than Fe are commonly referred to as “CEMP-no” stars.

To deal with this wide variety of compositions different scenarios for the origin of halo stars with peculiar compositions have been proposed. Halo stars showing pure  $r$  enhancements are believed to have been born from material heavily polluted by a primordial core-collapse supernova (SN of Type II, SNII) where the  $r$ -process elements are supposed to have formed. Though we note that there are still no SNII models able to reproduce the conditions needed for the  $r$  process to occur. One of the most favored sites to date, the neutrino wind from the nascent neutron star, has recently been shown to have major difficulties in producing  $r$ -process nuclei (Roberts et al. 2010). Qualitatively, the C and  $s$  enhancements in CEMP- $s$  and CEMP- $s/r$  stars can be explained by the presence of an originally more massive binary companion to the observed star, which produced C and  $s$ -process elements during its asymptotic giant branch (AGB) phase and transferred them to its companion via mass transfer, by either Roche-Lobe overflow or wind accretion (Lucatello et al. 2005). About 50% of CEMP stars showing an  $s$ -process signature also show an  $r$ -process signature and are thus classified as CEMP- $s/r$  stars. It is puzzling how CEMP- $s/r$  stars could have formed in such a large number given that we believe the  $s$  and the  $r$  processes to be independent events occurring in different astrophysical sites, AGB stars and SNII, respectively. Many scenarios have been proposed (as summarised by Jonsell et al. 2006; Lugaro et al. 2009) and most of them seem unlikely. Predictions from a scenario where the  $r$ -process enhancements are supposed to be primordial to the binary system have been investigated in detail by Bisterzo et al. (2011b) and will be discussed in § 4.1.

---

<sup>1</sup>The standard spectroscopic notation  $[X/Y] = \log_{10}(X/Y) - \log_{10}(X/Y)_{\odot}$  is used throughout this paper.

The N enhancements in CEMP stars are also mysterious. The highest enhancements,  $[N/C]>0$ , may be due to the effect of proton captures at the base of the convective envelope in AGB stars with masses higher than  $\simeq 3 M_{\odot}$  (hot bottom burning, HBB Lattanzio 1991; Boothroyd et al. 1993), which very efficiently convert C into N. The milder enhancements can be qualitatively explained by H and He burning occurring together when protons are ingested in the He-burning convective regions of AGB stars (Campbell & Lattanzio 2008; Iwamoto et al. 2004), or by the operation of some form of deep mixing of the envelope material of the AGB star companion down to regions where H burning occurs. No physical mechanism for this deep mixing has been shown to be capable of producing the required nitrogen enhancement. Stancliffe (2010) has shown that it cannot be caused by thermohaline mixing. Another issue that has received much attention is the question of whether material transferred from the AGB companion onto the star now observed as a CEMP star was diluted on the secondary star via thermohaline mixing (or any non-convective process), or kept at the surface until the star reached the giant branch and developed an extended convective envelope (Stancliffe et al. 2007; Stancliffe & Glebbeek 2008).

In this context, it is obvious that detailed models of the *s* process in AGB stars of low metallicity are crucial to improving our understanding of CEMP stars. Some models have been presented so far by Van Eck et al. (2003), Cristallo et al. (2009b), and Bisterzo et al. (2010) and have been compared to stellar observations by Bisterzo et al. (2011b,a). With this paper we greatly extend the range of published models of the *s* process in AGB stars by presenting the evolution and nucleosynthesis in a large set of stellar models of masses ranging from  $0.9 M_{\odot}$  to  $6 M_{\odot}$  at the typical metallicity of CEMP stars  $[Fe/H]=-2.3$ . The *s*-process predictions for low-metallicity AGB stars of masses lower than  $1.3 M_{\odot}$  and higher than  $2 M_{\odot}$  are provided here for the first time in the literature. To test different physical and numerical approaches we computed stellar evolutionary sequences using two different evolutionary codes. We then input these different evolutionary sequences into the same post-processing code, which employs a nuclear network from H to Bi and calculates nucleosynthesis by coupling mixing and burning in convective regions. We then compare our model predictions to the abundances of CEMP stars as a population using the recent compilation of CEMP star compositions from Masseron et al. (2010).

### 1.1. The *s* process in AGB stars of low metallicity

From centre to surface an AGB star consists of: a C-O degenerate core, a He-burning shell, a He-rich intershell, a H-burning shell, and an extended convective envelope, which is constantly eroded by strong stellar winds. When the whole envelope is lost the hot stellar

core is left to evolve into the post-AGB phase, then it becomes the central star of a planetary nebula and eventually a cooling white dwarf. For a detailed review on AGB evolution we refer the reader to Herwig (2005). A peculiarity of the AGB evolution is that the H- and the He-burning shells are activated alternately. Most of the time the H-burning shell is active and freshly made He increases the mass of the intershell for periods of time of around  $10^3$ - $10^5$  yr, depending on the stellar mass, with shorter periods associated with more massive AGB stars. The increasing mass of the intershell leads to an increase in the temperature at its base, until He burning is suddenly triggered resulting in a *thermal pulse* (TP). The energy released in this first phase of He-shell burning cannot be carried out radiatively and a convective region develops in the intershell, which lasts a few hundreds years (the exact duration depends on mass) and normally extends up to just below the H-burning shell. In low-mass and low-metallicity AGB stars this convective region can extend into the H-rich layer and peculiar nucleosynthesis is expected to occur there (Campbell & Lattanzio 2008), including *s*-process nucleosynthesis (Cristallo et al. 2009a). Mild proton-ingestion events of this type are found in our low-mass models. They have a strong impact on the *s*-process distributions and will be discussed in detail in § 3.

A TP causes the star to expand, which in turn causes the H-burning shell to be quenched. At this stage, the convective envelope can penetrate into the underlying layers and carry to the stellar surface material processed by H and He burning (a process referred to as the *third dredge-up*, or TDU for short), while He burning carries on radiatively. Eventually, He burning is also quenched and the whole cycle of H burning, TP, and TDU starts again. This cycle is repeated a few to hundreds of times depending on the time it takes for the mass loss to erode the envelope, which in turn depends on the initial stellar mass, and possibly the metallicity. The best evidence that TPs and the TDU occur in AGB stars is the formation of carbon stars, which show  $C > O$  at their surface as well as the presence of the radioactive element Tc (Wallerstein & Knapp 1998). This observed composition is explained by the combined effect of partial He burning during TPs (which produces more C than O) and the *s* process (which produces Tc), along with the TDU, which carries a fraction of the intershell to the stellar envelope. As mentioned above, HBB is present in AGB stars with masses higher than  $\simeq 3 M_{\odot}$  at the metallicity considered here, converting C into N.

The *s* process occurs in the intershell of AGB stars where He is abundant and ( $\alpha, n$ ) reactions can be efficiently activated. For a detailed review on the *s* process in AGB stars we refer the reader to Busso et al. (1999). There are two possible neutron sources: the  $^{13}\text{C}(\alpha, n)^{16}\text{O}$  and the  $^{22}\text{Ne}(\alpha, n)^{25}\text{Mg}$  reactions. The  $^{22}\text{Ne}$  neutron source is activated at temperatures higher than roughly  $300 \times 10^6$  K (hereafter MK). These high temperatures can only be reached inside the convective TPs, and mainly in AGB stars more massive than  $\simeq 3 M_{\odot}$  (Truran & Iben 1977). The  $^{22}\text{Ne}$  is produced via double  $\alpha$  captures on  $^{14}\text{N}$  when the H-

burning ashes are engulfed in the TP. The resulting neutron flux occurs over a timescale of the order of a few years with relatively high neutron densities, up to  $10^{14}$  n/cm<sup>3</sup> (Gallino et al. 1998; Lugaro et al. 2003; van Raai et al. 2011). The <sup>13</sup>C neutron source is instead activated at temperatures as low as 90MK (Cameron 1955) but there is not enough <sup>13</sup>C in the H-burning ashes of AGB stars to make it an efficient neutron source. Without this low-temperature neutron source it is not possible to explain the *s*-process enhancements which have been observed in AGB stars since the 1950s (Merrill 1952; Smith & Lambert 1986). This is because most of the observed *s*-process-enriched AGB stars are of relatively low mass ( $< 4 M_{\odot}$ ) where the temperature is not high enough to activate the <sup>22</sup>Ne neutron source. Thus, it has become standard practice to artificially include the <sup>13</sup>C neutron source in AGB models of the *s* process.

The most likely way to form the required <sup>13</sup>C is to allow some extra mixing of protons to occur following each TDU episode at the deepest extent of the convective envelope, where a sharp composition discontinuity forms at the interface between the H-rich envelope and the He-rich intershell. This extra mixing may be physically explained by the effect of semi-convection (Hollowell & Iben 1988), hydrodynamical overshoot (Herwig 2000; Cristallo et al. 2009b), or gravity waves (Denissenkov & Tout 2003). However, there is no agreement yet on which of these proposed mechanisms is responsible for the extra mixing and thus we do not know what its detailed features are. The protons are captured by the abundant <sup>12</sup>C, producing a layer rich in <sup>13</sup>C and <sup>14</sup>N (the <sup>13</sup>C *pocket*, Hollowell & Iben 1988; Gallino et al. 1998; Goriely & Mowlavi 2000; Lugaro et al. 2003; Cristallo et al. 2009b). The resulting <sup>13</sup>C usually burns under radiative conditions via <sup>13</sup>C( $\alpha$ ,n)<sup>16</sup>O before the onset of the following TP (Straniero et al. 1995; Gallino et al. 1998). This burning releases a large number of free neutrons on a long timescale (around  $10^4$  yr) and with low neutron densities  $< 10^8$  n/cm<sup>3</sup>. In the region of the pocket where <sup>14</sup>N is more abundant than <sup>13</sup>C, no *s*-process nucleosynthesis occurs owing to the dominance of the <sup>14</sup>N(n,p)<sup>14</sup>C reaction over neutron captures by Fe seed nuclei and their progeny. In the intermediate-mass AGB stars that experience HBB, the formation of a <sup>13</sup>C pocket may be inhibited by proton captures occurring at the hot base of the convective envelope during the TDU, which produce <sup>14</sup>N and not <sup>13</sup>C (Goriely & Siess 2004). Extremely deep TDU may also inhibit the activation of the <sup>13</sup>C( $\alpha$ ,n)<sup>16</sup>O reaction by penetrating into regions of the stellar core with a low abundance of <sup>4</sup>He (Herwig 2004a). While these processes do need further investigation, on first sight a dichotomy appears in models of the *s* process in AGB stars where the <sup>13</sup>C neutron source is activated in the low-mass models, while the <sup>22</sup>Ne neutron source is activated in the higher-mass models. At the metallicity we consider here the mass at which the importance of the two neutron sources switches is  $\simeq 3 M_{\odot}$  (Goriely & Siess 2004).

An interesting feature of the <sup>13</sup>C neutron source is that it is a primary neutron source

because it is produced from the H and He originally present in the stars. Since the total time-integrated neutron flux  $\tau$  from the  $^{13}\text{C}$  source is proportional to  $^{13}\text{C}/Z$ , the *s*-process predictions have a strong dependence on the metallicity of the star (Clayton 1988; Busso et al. 2001). Specifically, with  $\tau$  increasing when decreasing  $Z$ , heavier elements are produced at lower metallicities. This property allowed Gallino et al. (1998) to predict the existence of low-metallicity Pb-rich stars, which was confirmed by observations of Pb-rich CEMP stars (e.g., Van Eck et al. 2003). On the other hand, the  $^{22}\text{Ne}$  neutron source is traditionally considered to be a secondary neutron source, since it relies on the original CNO nuclei present in the star. However, at the low metallicities considered here  $^{22}\text{Ne}$  also has an important primary component because the N abundance in the H-burning ashes increases significantly from its initial value. This is due to the effect of TDU carrying primary  $^{12}\text{C}$  to the envelope, which is then converted into N by H burning.

The  $^{13}\text{C}$  and the  $^{22}\text{Ne}$  neutron sources produce neutron fluxes and neutron-capture nucleosynthesis with different features. In summary, it has been shown that the  $^{13}\text{C}$  source is responsible for the production of the bulk of the *s*-process elements in low-mass AGB stars reaching, as mentioned above, up to Pb at low metallicities (Gallino et al. 1998). Branching points on the *s*-process path are mostly closed during this neutron flux. The  $^{22}\text{Ne}$  source instead produces smaller abundances of the *s*-process elements but it efficiently activates branching points along the *s*-process path (Abia et al. 2001; van Raai et al. 2011). Note that at low metallicity  $^{22}\text{Ne}$  is both a neutron source and a neutron poison via  $(n,\gamma)$  reactions, leading to the production of light elements such as Na and Mg (Herwig 2004b; Karakas 2010; Bisterzo et al. 2010). Based on our models in § 3 we revise the different neutron-capture scenarios for AGB stars of low metallicity.

## 2. Stellar Models

The stellar evolutionary sequences were computed using the STARS and the Monash/Mount Stromlo (hereafter Stromlo) codes. The STARS code was originally written by Eggleton (1971) and has been updated by many authors (e.g. Pols et al. 1995; Stancliffe & Eldridge 2009). Mixing is treated via a diffusion equation (Eggleton 1972) and convective boundaries are determined via the Schwarzschild criterion. The opacities tables are from Eldridge & Tout (2004) and the nuclear reaction rates are from Stancliffe et al. (2005). Models are evolved from the pre-main sequence to the AGB using 999 mesh points. Mass loss before the AGB phase is included using the Reimers (1975) prescription, with  $\eta = 0.4$ . Mass loss during the AGB phase is included using the prescription of Vassiliadis & Wood (1993). The computation of the AGB phase with the STARS code has been described in detail in Stancliffe et al.

(2004). We included an approximate contribution to the molecular opacities (based on the work of Marigo 2002) that varies with envelope composition (Stancliffe & Glebbeek 2008). Convective overshooting is not included at any stage in the evolution, and a mixing length of  $\alpha = 2.0$  is employed throughout.

The Stromlo code uses the standard mixing-length theory for convective regions, with a mixing-length parameter  $\alpha = 1.75$ , and determines the border of convective regions by applying the Schwarzschild criterion. Convective overshooting is not employed at any stage in the evolution, although the code searches for a neutral border to the convective zone in the same way as described in Lattanzio (1986). This can have the effect of increasing the efficiency of the TDU (Frost & Lattanzio 1996; Karakas et al. 2002). At high temperatures the OPAL opacities are used (Iglesias & Rogers 1996), and at low temperatures (below  $T \leq 10^4\text{K}$ ) two different prescriptions are employed. The models between 1 to  $2.5M_{\odot}$  (Karakas & Lattanzio 2007) include an approximate treatment for the molecular opacities (in particular CN, CO, H<sub>2</sub>O, TiO) using the formulations from Bessell et al. (1989) and corrected by Chiosi et al. (1993). These fits do include some compositional dependence, but do not account for large variations in the envelope C/O ratio or N abundance. In the model of  $0.9 M_{\odot}$  and models between 3 to  $6 M_{\odot}$  the code uses the (scaled-solar) low-temperature opacity tables from Ferguson et al. (2005) in place of the Bessell et al. (1989) fits. Mass loss before the AGB phase is included using the Reimers (1975) prescription, with  $\eta = 0.4$ . For the models between  $0.9$  to  $2.5 M_{\odot}$  mass loss during the AGB phase is included using the prescription of Vassiliadis & Wood (1993). For models of 3 to  $6 M_{\odot}$  mass loss during the AGB is included using the Reimers (1975) prescription with  $\eta$  values that vary with mass (see discussion in Karakas 2010).

Two further Stromlo models of  $2 M_{\odot}$  and  $2.5 M_{\odot}$  of  $Z = 0.0001$  were calculated using the low-temperature C and N-rich opacities from Lederer & Aringer (2009). These new stellar evolutionary sequences were computed with Vassiliadis & Wood (1993) mass loss on the AGB and updated reaction rates for the  $^{14}\text{N}(p, \gamma)^{15}\text{O}$  reaction (the LUNA rate from Bemmerer et al. 2006), and the NACRE rate for the triple- $\alpha$  process (Angulo et al. 1999). These models were computed to quantitatively test the effect of the low-temperature opacity tables on the evolution of low-metallicity AGB stars, in particular to reconcile the number of TPs obtained between the Stromlo and the STARS models. Many of the important features of the new models are the same as the old models, including the maximum depth of the TDU, however, the main change is a reduction in the number of TPs and hence the total amount of He-shell material dredged to the envelope over the AGB phase. One interesting feature of the new models is that they were both evolved to the white dwarf cooling track, where the final envelope masses are a few  $\times 10^{-5} M_{\odot}$ , providing an excellent estimate of the total number of predicted TPs.



All our models were computed using a metallicity of  $[\text{Fe}/\text{H}]=-2.3$ . The peak of the distribution of the metallicities of CEMP stars enhanced in neutron-capture elements is at  $[\text{Fe}/\text{H}]=-2.3$  and the overall range cover  $-3.5 < [\text{Fe}/\text{H}] < -1$ . (see, e.g., Fig. 7 of Aoki et al. 2007). Keeping this caveat in mind, we will compare our models to the composition of CEMP stars as a population, rather than to single objects.

The main features of our stellar models are presented in Fig. 1, and Tables 1 and 2. The tables include: the initial stellar mass, the total number of thermal pulses (TPs), which thermal pulses are followed by the TDU (TPs with TDU), the maximum temperature in the TPs followed by the TDU ( $T_{\text{He}}^{\text{max}}$ , also plotted in the bottom panel of Fig. 1), the maximum TDU efficiency  $\lambda_{\text{max}}$ , defined as the ratio of the mass scooped up to the envelope by the TDU over the mass growth of the H-exhausted core in the previous interpulse phase, the total mass dredged-up by TDU during the TP-AGB (total  $M_{\text{dred}}$ , also plotted in the upper panel of Fig. 1), the mass of the envelope at the end of the computed evolution (final  $M_{\text{env}}$ ), if HBB is at work or not, and the maximum temperature at the base of the convective envelope. The main features arising from the analysis of the two sets of models are:

1. The number of TPs (Column 2) is smaller - roughly half at any given initial mass (Column 1) - in the STARS code than in the Stromlo code. This is because the STARS code includes an approximation to the molecular opacities that varies with the composition of the envelope. This is known to affect the mass-loss rates and shorten the stellar lifetime (Marigo 2002). The Stromlo  $2 M_{\odot}$  and  $2.5 M_{\odot}$  models computed using low-temperature opacities with varied C and N abundances from Lederer & Aringer (2009) experienced  $\simeq 40\%$  fewer TPs thus confirming the effect of shortening the stellar lifetime when more realistic low-temperature opacities are used. The  $2 M_{\odot}$  model of the same metallicity presented by Cristallo et al. (2009b) uses the same molecular opacities from Lederer & Aringer (2009), but a slightly different mass-loss law and has 15 TPs, close to the number of TPs in our  $2 M_{\odot}$  models.
2. While the overall trend is for the number of TPs to increase with initial stellar mass (as a larger envelope means that it takes more time for the mass loss to erode it), models with masses lower than  $1.25 M_{\odot}$  show instead an increase in the number of TPs. We obtain a higher total TDU mass and a higher intershell temperature in the  $0.9 M_{\odot}$  model than in the  $1 M_{\odot}$  models. This result is most likely to be affected by uncertainties in the mass-loss rate, which are large, and needs to be investigated in more detail. In the lowest-mass models the initial pulses are too weak to trigger efficient TDU (Column 3), and thus  $\text{C}/\text{O} > 1$  is reached later during the evolution.
3. The fact that the STARS models experience fewer TPs with TDU (Column 3) than the Stromlo models leads to a smaller amount of dredged up material being mixed into the

envelope over the AGB phase (Columns 6). This is illustrated in Fig. 1. The exception to this is the  $1 M_{\odot}$  model. The total TDU mass does not change linearly with the number of TPs because it is also determined by the numerical treatment of the inner border of the convective envelope, which differs in the two codes. More efficient TDU is typically favored in the STARS models (Column 5).

4. The maximum temperature reached in TPs followed by the TDU (Column 4) is lower in the STARS models than in the Stromlo models (except for the STARS  $1 M_{\odot}$  model, which has more TDU episodes). The  $^{22}\text{Ne}(\alpha, n)^{25}\text{Mg}$  reaction starts to operate at temperatures of  $\simeq 300$  MK, which is reached in the  $1.9 M_{\odot}$  Stromlo model and in the  $2.5 M_{\odot}$  STARS model. This quantity is also known to increase with the TP number.
5. The final envelope mass is mostly determined by how long we managed to run the codes before encountering insurmountable convergence problems, usually during the final phase of very high mass loss that is typical of the prescription of Vassiliadis & Wood (1993) we used. It is usually easier to get closer to the end of the AGB phase with models of lower masses, although the intermediate-mass evolutionary sequences computed by the Stromlo code were also evolved to small (around  $0.1 M_{\odot}$ ) envelope masses probably due to the choice of the Reimers (1975) mass loss prescription on the AGB, instead of Vassiliadis & Wood (1993). For these models we do not expect any further TPs and TDU episodes, except perhaps at the very tip of the AGB or during the post-AGB phase.
6. The minimum mass at which we see the operation of HBB is  $3 M_{\odot}$ , the same for both codes. HBB is very mild in this Stromlo model, with a maximum temperature at the base of the convective envelope  $\simeq 40$  MK (Column 8), while it is more efficient for the STARS ( $T_{\text{bce}}^{\text{max}} \simeq 58$  MK). HBB is already very efficient for the  $3.5 M_{\odot}$  Stromlo model, with a maximum temperature  $\simeq 76$  MK.
7. The Stromlo models with mass  $> 3 M_{\odot}$  reach temperatures in the He-burning shell up to 378 MK. These temperatures are high enough for an efficient activation of the  $^{22}\text{Ne}$  neutron source. The total TDU mass dredged up is similar in all intermediate-mass models, with a slight trend to increase with increasing stellar mass due to the increasing number of TPs.

We note that most of the quantities presented in Tables 1 and 2 are affected by uncertainties related to the treatment of the TDU and to the mass-loss rate.

## 2.1. Nucleosynthesis models

To study the nucleosynthesis of the elements up to Bi we have used a post-processing code that takes as input the stellar evolutionary sequences described above. The stellar inputs are the temperature, density, and convective velocities (for convective regions) at each mass shell in the star as a function of time during the life of the star. Convective velocities are needed because the code includes both the changes due to nuclear reactions and those due to mixing in the equations to be solved for the abundances. An implicit method is used to solve  $N$  equations,  $N$  being the number of species included in the nuclear network, by inverting a large matrix containing  $N^2$  elements. The code has been previously described in detail by, e.g., Cannon (1993), Karakas & Lattanzio (2007), and Lugaro et al. (2004).

Given that the number of species  $N$  determines how large the matrix to be solved is, in the interest of making the computation relatively fast (from a few days to a few weeks, depending on the initial stellar mass), we used for this work a basic  $s$ -process network, where we included a total of 320 species mostly along the valley of  $\beta$  stability, and 2,336 reactions. We based our nuclear reaction network on the JINA REACLIB database, as of May 2009. From this database, we updated the rates for the neutron source reactions: we took the  $^{13}\text{C}(\alpha, n)^{16}\text{O}$  rate from Heil et al. (2008) and the  $^{22}\text{Ne}(\alpha, n)^{25}\text{Mg}$  from Karakas et al. (2006).

For the initial composition of most models we used the solar distribution of abundances from Asplund et al. (2009) scaled down to  $[\text{Fe}/\text{H}]=-2.3$ . Solar abundances of C, N, O, Ne, Mg, Si, S, Ar, and Fe are the pre-solar nebula values from Table 5 of Asplund et al. (2009); F is the meteoritic value of  $\log \epsilon (F)_{\odot} = 4.42$  from Table 1 of the same paper (chosen because it has a lower uncertainty), and for many of the elements heavier than Fe we use the meteoritic values for the solar abundances (e.g., Sr, Eu, Pb).

We also computed some models by varying the initial composition to: (1) the values predicted by galactic chemical evolution models for solar neighborhood stars of metallicity  $[\text{Fe}/\text{H}]=-2.3$  from Kobayashi et al. (2011), this case affects only the initial composition of the elements up to Zn; (2) the values obtained assuming that the star was born with an  $r$ -process enrichment and in some cases also an  $s$ -process enhancement. Enhancements in the initial  $r$ -process abundances may have arisen from the pollution from one or a few primordial SNeII. Enhancements in the initial  $s$ -process abundances may have arisen from pollution from primordial massive stars producing  $s$ -process elements during core He and shell C burning (Pignatari et al. 2008), or via the still unidentified “light element primary process” (Travaglio et al. 2004; Montes et al. 2007). To compute these  $r$  and  $s$ -process enhancements we used the  $s$  and  $r$  contributions given in Sneden et al. (2008).

## 2.2. The inclusion of the $^{13}\text{C}$ pocket

The methodology for the inclusion of the  $^{13}\text{C}$  pocket deserves specific attention as the formation of this neutron source is still the main uncertainty in the  $s$ -process models. For reasons discussed above (§ 1.1), we introduced a  $^{13}\text{C}$  pocket for models of masses  $< 4 M_{\odot}$ , while we did not introduce it for the higher masses, except in one test case, where we introduced a  $^{13}\text{C}$  pocket in the Stromlo  $5.5 M_{\odot}$  model. Also the  $3 M_{\odot}$  model was computed with and without the inclusion of the  $^{13}\text{C}$  neutron source to illustrate in detail the different effects of the two neutron sources. This mass lies where the two regimes switch: the  $s$ -process dominated by the  $^{13}\text{C}$  neutron source and the  $s$ -process dominated by the  $^{22}\text{Ne}$  neutron source.

The inclusion of the  $^{13}\text{C}$  neutron source was performed artificially during the post-processing by forcing the code to mix a small amount of protons from the envelope into the intershell at the deepest extent of each TDU episode. All the studies to date investigating the formation of the  $^{13}\text{C}$  pocket by various mechanisms have found that the proton abundance in the intershell decreases monotonically. Hence, we apply the basic assumption that the proton abundance in the intershell decreases monotonically from the envelope value of  $\simeq 0.7$  to a minimum value of  $10^{-4}$  at a given point in mass located at “ $M_{\text{mix}}$ ” below the base of the envelope. This method is described in some more detail in Lugaro et al. (2004) and is very similar to that used by Goriely & Mowlavi (2000). We made the further choice that the proton abundance decreases exponentially, i.e., linearly in a logarithmic scale. Studies of the formation of the  $^{13}\text{C}$  pocket have found profiles that can slightly differ from this basic assumption, as well as from each other. For example, compare the profile shown in Fig. 4 of Herwig (2000) to the profiles shown in Figs. 1-4 of Cristallo et al. (2009b). Goriely & Mowlavi (2000) tested the effect of using a “slow” or a “fast” profile (see their Fig. 10) and found no major differences in the  $s$ -process distribution.

We tested different values of our parameter  $M_{\text{mix}}$ , representing the extent in mass of the proton profile. The extent in mass of the resulting  $^{13}\text{C}$  pocket is  $< M_{\text{mix}}$  (Goriely & Mowlavi 2000; Lugaro et al. 2003; Cristallo et al. 2009a). For some models of mass  $< 3 M_{\odot}$  we tested  $M_{\text{mix}}=0, 0.0006 M_{\odot}, 0.001 M_{\odot}, 0.002 M_{\odot},$  and  $0.004 M_{\odot}$ . For the  $3 M_{\odot}$  models we used  $M_{\text{mix}}= 0, 0.0005 M_{\odot}$  and  $0.001 M_{\odot}$ . For the  $5.5 M_{\odot}$  model, we tested  $M_{\text{mix}}=0$  and  $0.0001 M_{\odot}$ . To keep the standard assumption that the  $^{13}\text{C}$  pocket should be a minor fraction ( $\simeq 1/10 - 1/20$ ) of the intershell mass (Gallino et al. 1998; Goriely & Mowlavi 2000) we had to decrease the value of  $M_{\text{mix}}$  with the stellar mass because the mass of the intershell is at least an order of magnitude smaller in the intermediate-mass AGB stars than in the lower-mass models: around  $10^{-2} M_{\odot}$  in a  $1.5 M_{\odot}$  model compared to around  $10^{-3} M_{\odot}$  in a  $6 M_{\odot}$  model.

### 3. Results

The results in terms of  $[X/Fe]$  for selected key elements (where X represent a given element) for all our models are presented in Tables 3 and 4 and Figs. 2 and 3<sup>2</sup>. The elemental abundances  $[X/Fe]$  in these tables are given at the stellar surface at the end of the computed evolution. The extended tables available on-line list, for each element X included in the network:  $\log \epsilon(X)$ , i.e.,  $12 + \log_{10} \{N(X)/N(H)\}$ ,  $[X/H]$ ,  $[X/Fe]$ , and  $[X/O]$ , and  $X(i)$ , which is the fraction of element i by mass at the surface. We also include the C/O ratio and the isotopic ratios of C, N, O, and Mg. All elemental and isotopic ratios are number ratios. These quantities are tabulated at the stellar surface at the start of the evolution, after each TP, and at the end of the evolution, accounting for the radioactive decay of long-lived isotopes.

We also present in the extended tables and in the figures of § 4 the *s*-process indices light “ls” and heavy “hs”. We choose the three main elements belonging to the first *s*-process peak Sr, Y, and Zr to define  $[ls/Fe]=([Sr/Fe]+[Y/Fe]+[Zr/Fe])/3$  and the three main elements belonging to the second *s*-process peak Ba, La, and Ce to define  $[hs/Fe]=([Ba/Fe]+[La/Fe]+[Ce/Fe])/3$ . We choose these definitions to compare our models to the data from the compilation of Masseron et al. (2010), who report abundances for Ba, La, Ce, Eu, and Pb<sup>3</sup>. We note that our definitions are different from those used by Bisterzo et al. (2010) who took Y and Zr as the ls elements, and La, Nd, and Sm, as the hs elements. That choice was made in order to select the elements for which spectroscopic determinations are more reliable<sup>4</sup>. In the extended on-line tables we provide  $[ls/Fe]$  and  $[hs/Fe]$  as defined in this work and as defined by Bisterzo et al. (2010), for comparison.

We have identified four different regimes of neutron captures in our models, which explain the different abundance distributions for the elements heavier than Fe in Fig. 2, corresponding to the different  $[Ba/Sr]$  and  $[Pb/Ba]$  ratios listed in Table 3 and 4. These regimes are described below, together with the typical stellar mass ranges at which they occur. The mass range in which each regime is at work is slightly different in the two sets of models, STARS and Stromlo and in most models more than one regime is at work. In principle the final results depend on the interplay of the different regimes, though often a dominant situation can be identified. The regimes are:

---

<sup>2</sup>We had numerical problems computing the nucleosynthesis for the STARS 1  $M_{\odot}$  model, which we still have not manage to solve, so the results of this model are not included in the tables and figures.

<sup>3</sup>For data on the ls elements we searched the SAGA database (Suda et al. 2008).

<sup>4</sup>Note that, according to Arlandini et al. (1999), about 80% of the solar abundances of Sr, Y, Zr, Ba, and Ce are produced by the *s* process, while La, Nd, and Sm have an important *r*-process contribution: 62%, 56%, and 29% of their solar abundances are ascribed to the *s* process, respectively.

1. *The  $^{22}\text{Ne}(\alpha,n)^{25}\text{Mg}$  neutron source operates inside TPs when the temperature at the base of the TP reaches above 300 MK.* From Fig. 1 it is clear that this neutron source operates when the initial stellar mass is higher than about  $2 - 2.5 M_{\odot}$ . Two key features of this regime are that (i) the temperature is never high enough to completely burn the  $^{22}\text{Ne}$  nuclei (at most the  $^{22}\text{Ne}$  intershell abundance decreases by a factor of three) and (ii) the neutrons are distributed over the whole intershell by the convective TP. The resulting overall number of neutrons per Fe seed produces distributions where lighter  $s$ -process elements are favored with respect to heavier  $s$ -process elements. For this reason the [Ba/Sr] and [Pb/Ba] ratios are negative. The neutron density reaches up to  $\simeq 10^{14}$  n/cm<sup>3</sup>, so branching points are affected but the overall distribution is a typical  $s$ -process distribution. In our models the activation of the  $^{22}\text{Ne}$  neutron source in intermediate-mass AGB stars does not lead to an enhanced production of Eu, as was suggested by Masseron et al. (2010). The [Ba/Eu] ratio in these models remains close to unity<sup>5</sup>. This is the value expected by the  $s$  process in equilibrium with  $\sigma_A N_A = \text{constant}$ , where  $\sigma_A$  is the neutron-capture cross section of the isotope of mass A and  $N_A$  is its  $s$ -process abundance, considering that the neutron-capture cross section of, e.g., the neutron magic nucleus  $^{138}\text{Ba}$  is  $\sim 650$  times lower than the neutron-capture cross section of, e.g.,  $^{153}\text{Eu}$ , while its solar abundance is  $\sim 65$  times higher<sup>6</sup>.
  
2. *The  $^{13}\text{C}(\alpha,n)^{16}\text{O}$  neutron source operates in radiative conditions during the interpulse periods, with  $^{13}\text{C}$  produced by the inclusion of a  $^{13}\text{C}$  pocket (cases with  $M_{\text{mix}} \neq 0$ ).* Typical models where this is the main regime of neutron captures are the models with initial masses between roughly  $1.75 M_{\odot}$  and  $3 M_{\odot}$ . Two key features of this regime are that (i) the  $^{13}\text{C}$  nuclei burn completely in radiative conditions and (ii) the neutrons are captured locally in the thin  $^{13}\text{C}$ -pocket layer. The overall number of neutrons per Fe seed produces  $s$ -process distributions weighed towards Pb, with [Pb/Ba] ratios in some cases exceeding unity and  $0 < [\text{Ba}/\text{Sr}] < 1$ . In the massive  $5.5 M_{\odot}$  model the only effect of including the  $^{13}\text{C}$  pocket is the increase in the production of Pb by a factor of  $\simeq 50$ , so that this is the only massive AGB model where the final [Pb/Ba] ratio is positive. Efficient activation of the  $^{13}\text{C}$  neutron source produces [Ba/Eu] ratios close to unity, which is typical of the  $s$  process and similar to what was found for Regime

---

<sup>5</sup>The [Ba/Eu] ratio decreases down to 0.11 only in the  $3 M_{\odot}$  STARS model computed without the inclusion of the  $^{13}\text{C}$  pocket, but this is due to the fact that not much  $s$  process occurs here so that very little Ba and no Eu are produced in this model.

<sup>6</sup>We can approximately apply the  $\sigma_A N_A = \text{constant}$  rule because the Eu abundance in  $s$ -process conditions follows that of Ba, the magic nuclei that precedes it in mass.

- 1.
3. *The  $^{13}\text{C}(\alpha,n)^{16}\text{O}$  neutron source operates in convective conditions, with  $^{13}\text{C}$  produced by the inclusion of a  $^{13}\text{C}$  pocket (cases with  $M_{\text{mix}} \neq 0$ ).* In this case the  $^{13}\text{C}$  in the  $^{13}\text{C}$  pocket does not completely burn radiatively and is ingested in the following TP. This regime characterises the first two or three  $^{13}\text{C}$  pockets in the lowest mass models, e.g., in the  $1.25 M_{\odot}$ , and  $1.5 M_{\odot}$  models the first three  $^{13}\text{C}$  pockets are engulfed in the following TPs while the abundance of  $^{13}\text{C}$  is still higher than  $10^{-4}$  (by number), and it is close to  $10^{-3}$  for the first  $^{13}\text{C}$  pocket. In the  $1 M_{\odot}$  Stromlo model we find two TDU episodes and thus two  $^{13}\text{C}$  pockets are included (cases with  $M_{\text{mix}} \neq 0$ ), both of which are ingested in the following TP while the abundance of  $^{13}\text{C}$  is still higher than  $10^{-4}$ . The neutrons are released over material in the whole intershell region and the  $^{13}\text{C}$  is mixed with the  $^{14}\text{N}$  poison from the  $^{13}\text{C}$  pocket and from the H-burning ashes. Thus, the number of neutrons per Fe seed is lower with respect to the case when  $^{13}\text{C}$  burns completely in radiative conditions. Consequently, the [Pb/Ba] ratio is also lower.
4. *The  $^{13}\text{C}(\alpha,n)^{16}\text{O}$  neutron source operates in convective conditions, with  $^{13}\text{C}$  produced by the ingestion of a small number of protons in the TPs.* This event occurs in the first few TPs in models with masses roughly less than  $2.5 M_{\odot}$ . The convective TP reaches at most the point in mass where the H mass fraction is 0.01 and we never find a splitting of the convective TPs as is seen to occur at lower metallicities and/or in other studies (e.g., Campbell & Lattanzio 2008; Cristallo et al. 2009a; Lau et al. 2009; Suda & Fujimoto 2010). However, the modeling of the proton ingestion event strongly depends on the treatment of convection and the convective mixing scheme employed. In the Stromlo code we instantaneously mix convective regions at each iteration, which is not appropriate in cases such as proton ingestion episodes when mixing and burning timescales are comparable. In the STARS code we use a diffusive mixing scheme (Eggleton 1972), which would be able to resolve the splitting of the convective region if it occurred. On the other hand, the first 3D simulations of AGB proton ingestion episodes considered here suggest that an advective mixing scheme may be more appropriate than a diffusive mixing scheme and that the splitting of the convective TP does not occur (Stancliffe et al. 2011). With these caveats in mind, we find that proton ingestion episodes can be expected to lead to favorable conditions for *s*-process nucleosynthesis and to favour the production of the *s*-process elements lighter than Pb, for the same reasons related to Regime 3 discussed above. While for models with mass higher than  $\simeq 1.9 M_{\odot}$  the effect of these events is dwarfed by the presence of the  $^{13}\text{C}$  pocket, in the lower mass models the proton-ingestion events alone can result in significant production of *s*-process elements (cases with  $M_{\text{mix}}=0$ ). The results are relatively low [Pb/Ba] ratios and the usual *s*-process [Ba/Eu] ratio near

unity. The final [Ba/Sr] in these low-mass models depends on the detailed features of the proton-ingestion episodes, with ingestion of a smaller number of protons favouring the production of Sr, as well as on the amount of  $^{13}\text{C}$  from the pocket that is left over to burn in the following TP (Regime 3). In some of the STARS models the final result is a negative [Ba/Sr] ratio. Production of the light element Na due to the  $^{22}\text{Ne}+\text{p}$  during the proton-ingestion events occurs in most of the low-mass models (cases with  $M_{\text{mix}}=0$ ).

As outlined above, the Stromlo and STARS models differ with regards to the masses at which the neutron-capture regimes are predominant. Thus, the relative distribution of the *s*-process elements (the [Ba/Sr] and [Pb/Ba] ratios) may be different for models of the same stellar mass (compare, e.g., the distributions plotted in Fig. 2 for the Stromlo and STARS models of same mass  $1.25 M_{\odot}$ .) The other main difference is that the absolute abundances with respect to Fe are typically smaller in the STARS than in the Stromlo models. This is because, as discussed in § 2, the STARS models have a smaller number of TDU episodes due to the inclusion of realistic molecular opacities which vary with the envelope composition and which result in a shorter AGB lifetime. The same effect, though to a smaller extent, appears when considering the Stromlo  $2 M_{\odot}$  and  $2.5 M_{\odot}$  models computed with the inclusion of molecular opacities.

We changed the initial abundances in most of our nucleosynthesis post-processing models according to the different choices indicated in § 2.1 and did not find any remarkable difference in the any of the final abundances reported in Tables 3 and 4 (as well as in Table 5 discussed below). The only significant change occurred to [Eu/Fe] when we applied a significant *r*-process enhancement. This is obvious as Eu is a predominantly *r*-process element. For example, in the Stromlo  $2 M_{\odot}$  model computed with  $M_{\text{mix}}=0.002 M_{\odot}$ , using an *r*-process contribution to the initial composition of  $[r/\text{Fe}]=0.0, 0.4, 1.0,$  and  $2.0$  dex, we obtained final [Eu/Fe]=1.51, 1.53, 1.60, and 2.08, respectively. In all cases, the [Ba/Fe] was unaffected, leading to final [Ba/Eu]=0.91, 0.89, 0.82, and 0.39, for the four cases respectively.

### 3.1. The light elements: C, N, O, F, Ne, Na, and Mg

The C, N, O, and F abundances in low-metallicity AGB stars have been already extensively presented by Herwig (2004b), Karakas & Lattanzio (2007), Lugaro et al. (2008), Stancliffe (2009) and Karakas (2010) so here we only discuss them briefly. In Fig. 3 we present the final [X/Fe] for the elements lighter than Fe for the same selected models of Fig. 2. In Table 5 we present the final [X/Fe] for C, N, O, F, and Ne for all our models and the indicated choices of  $M_{\text{mix}}$ . These light elements mostly do not change when varying this



free parameter: the only exceptions are for F and Ne. For example, F decreases by 0.41 dex and Ne by 0.45 dex in the Stromlo  $1 M_{\odot}$  model when  $M_{\text{mix}}=0$ . All our models are very rich in carbon and relatively poor in nitrogen, with typical  $[\text{C}/\text{N}]$  varying from  $\simeq 1$  dex, for the  $0.9$  and  $1 M_{\odot}$  models, to  $\simeq 2$  dex for models up to  $3 M_{\odot}$  (Fig. 3). From this stellar mass and above, HBB is activated and the nitrogen abundance increases and quickly overcomes the abundance of carbon. Oxygen is produced in our models, ranging from 0.42 to 1.34 dex. A typical product of AGB nucleosynthesis is fluorine, which we find to be strongly produced in our models:  $[\text{F}/\text{Fe}]$  is comparable to  $[\text{C}/\text{Fe}]$  up to the stellar mass where HBB is efficient. For higher masses fluorine is destroyed by proton captures. Neon is also a typical product of AGB stars, in the form of  $^{22}\text{Ne}$ , and its production factor varies in our models from  $\sim +1$  to  $\sim +3$  dex (Karakas & Lattanzio 2003). This element is observable in planetary nebulae and can be used as a further probe of AGB nucleosynthesis. The Ne abundance was derived for the halo planetary nebula BoBn 1, which is also rich in C, N, and F, and can be explained by low-metallicity AGB models of  $\approx 1.5 M_{\odot}$  (Otsuka et al. 2010). The production of F and Ne is primary in low-metallicity AGB stars because it is driven by the TDU of  $^{12}\text{C}$ . Our  $2 M_{\odot}$  models produce very similar results to the model of Cristallo et al. (2009b).

The light elements Na and Mg require specific discussion because they depend on the abundance of  $^{22}\text{Ne}$ , which in turn depends on the amount of TDU and therefore on the stellar mass, on the formation of the  $^{13}\text{C}$  pocket, and on the overall neutron flux. Our predictions for these elements are shown in Fig. 3 for selected models and listed in Tables 3 and 4 for all the models. Na is strongly produced in our models due to proton and neutron captures on  $^{22}\text{Ne}$ . For models without HBB, the increasing efficiency of the TDU with stellar mass means that the amount of primary  $^{22}\text{Ne}$  and Na in the envelope also increase with mass up to  $\simeq 2 M_{\odot}$ ; this is illustrated in Fig. 3. In these low-mass models the  $^{23}\text{Na}$  is synthesized by proton captures on  $^{22}\text{Ne}$  during both the interpulse and convective TP (see also Goriely & Mowlavi 2000; Cristallo et al. 2009b). Neutron captures on  $^{22}\text{Ne}$  occur any time there are neutrons available given the large abundance of  $^{22}\text{Ne}$  present in the intershell (see also the discussions in Karakas 2010; Bisterzo et al. 2010). In models of masses higher than around  $2 M_{\odot}$ , less Na is produced because the total amount of TDU as well as  $M_{\text{mix}}$  are smaller and because Na production by HBB is sensitive to mass. Na production requires higher temperatures than CNO cycling and takes place most efficiently at  $\approx 4 M_{\odot}$ ; at higher masses the temperature at the base of the envelope is so high that the Na is effectively destroyed by proton captures. At the other end of our mass range, in the lowest-mass models  $0.9$  and  $1 M_{\odot}$ , we also obtain a range of Na abundances, depending on the features of the proton ingestion and the inclusion of the  $^{13}\text{C}$  pocket. The  $0.9 M_{\odot}$  and  $1.0 M_{\odot}$  Stromlo models are the only models to have  $[\text{Na}/\text{Fe}]$  significantly lower than  $[\text{Ba}/\text{Fe}]$ . In all the other models  $[\text{Na}/\text{Fe}]$  is comparable and even higher than  $[\text{Ba}/\text{Fe}]$ .

Magnesium is also significantly produced in our models when the mass is greater than  $\simeq 1.25 M_{\odot}$ . In the models with mass lower than  $\simeq 2.5 M_{\odot}$  all the isotopes of Mg are produced via neutron captures in the  $^{13}\text{C}$  pocket starting on  $^{23}\text{Na}$ . For this reason the abundance of Mg follows the abundance of Na, keeping roughly to one order of magnitude lower than Na. In the models with mass higher than  $\simeq 2.5 M_{\odot}$ , the heavier isotopes of Mg,  $^{25}\text{Mg}$  and  $^{26}\text{Mg}$ , are also produced by  $\alpha$ -capture during the TP via the  $^{22}\text{Ne}+\alpha$  reactions. HBB in the most massive models leads to activation of the Mg-Al chains, which produces  $^{26}\text{Mg}$  and  $^{26}\text{Al}$  and alters the composition of the He-shell prior to each TP (Karakas & Lattanzio 2003). In these higher mass models the abundance of Mg becomes comparable to, and even larger than, that of Na.

In Fig. 4 we show the Mg isotopic ratios at the stellar surface at the end of the computed evolution. These ratios vary by up to three orders of magnitude with the stellar mass. The derivation of the the Mg isotopic ratios from the spectra of CEMP stars would represent very strong constraints on the mass of the donor AGB star. We note that the models shown in Fig. 4 were computed using the solar ratios of  $^{24}\text{Mg}/^{25}\text{Mg}=7.9$  and  $^{24}\text{Mg}/^{26}\text{Mg}=7.2$ . In selected models with mass  $\geq 1.5 M_{\odot}$  we tested the effect of starting with ratios derived from the detailed Galactic chemical evolution models of Kobayashi et al. (2011), i.e.,  $^{24}\text{Mg}/^{25}\text{Mg}=158$  and  $^{24}\text{Mg}/^{26}\text{Mg}=179$ . While this did not have any impact on the final ratios for the masses considered, the final compositions of stars with masses lower than  $1.5 M_{\odot}$  may be more strongly effected by the initial composition. This is because these models experience less dredge-up and for this reason, the final Mg isotopic ratios are likely to be higher than given here.

### 3.2. Comparison with previous models

In Table 6 we present a comparison of our results with those of Cristallo et al. (2009b) and Bisterzo et al. (2010) for the same element ratios as shown in Tables 3 and 4. The results from the STARS and Cristallo’s  $2 M_{\odot}$  models show very good agreement, both in the light (see Table 5) and in the heavy elements. Both these models were computed with the inclusion of molecular opacities. The Stromlo  $2 M_{\odot}$  models both with and without inclusion of realistic molecular opacities produces higher abundances of both light and heavy elements in AGB models, with respect to Fe. Varying the mass of the  $^{13}\text{C}$  pocket can also lead to significant changes in the predicted abundances of both light and heavy elements in AGB models. The model by Cristallo et al. (2009b) includes the  $^{13}\text{C}$  pocket using a self-consistent approach based on convective overshooting motivated by hydrodynamical simulation of convective/radiative boundaries. These authors found that the extent in mass of the pocket

decreases with the TP number. In our models instead we kept  $M_{\text{mix}}$  constant with the TP number. This explains why the abundances with respect to Fe by Cristallo et al. (2009b) are closer to those computed with the smaller  $M_{\text{mix}}$  value in our models. In any case, the ratios  $[\text{Ba}/\text{Sr}]$ ,  $[\text{Ba}/\text{Eu}]$ , and  $[\text{Pb}/\text{Ba}]$  are very similar in all three sets of models. This comparison indicates that the  $s$ -process distributions obtained using our artificial treatment of the  $^{13}\text{C}$  pocket are in agreement with those obtained using the self-consistent treatment of Cristallo et al. (2009b).

Bisterzo et al. (2010) treated the neutron production in the  $^{13}\text{C}$  pocket as a free parameter and varied its efficiency with respect to their standard (ST) case, which reproduces the solar system  $s$ -process abundances at  $Z = 0.01$ . This approach results in a larger allowed range of variations of the resulting abundances. The results from the Stromlo, STARS, and Cristallo’s models are typically included within the range predicted by Bisterzo et al. (2010).

Overall, Table 6 presents a relatively consistent set of results for neutron-capture nucleosynthesis in AGB stars of low metallicity. The main features of these models are the production of  $s$ -process elements up to +3 dex and a variety of  $s$ -process distributions, typically with  $0 < [\text{Ba}/\text{Sr}] < 1.0$ ,  $[\text{Ba}/\text{Eu}] \simeq 0.9$ , and  $0 < [\text{Pb}/\text{Ba}] < 2.0$ .  $[\text{Ba}/\text{Eu}]$  reaches lower values only if there is not a large  $s$ -process enhancement, i.e.,  $[\text{Ba}/\text{Fe}] < 1.0$ . The “radiative + convective” model of Goriely & Siess (2005) produces a heavy-element distribution in the range displayed in Table 6, with  $[\text{Ba}/\text{Sr}] \simeq 0.9$ ,  $[\text{Ba}/\text{Eu}] \simeq 0.8$ , and  $[\text{Pb}/\text{Ba}] \simeq 1.0$ , see their Fig. 6. The production of Na and Mg always increases with the stellar mass, something also seen in the Bisterzo et al. (2010) models. Their  $1.3 M_{\odot}$  models produce lower Na than the  $1.25 M_{\odot}$  models presented here because these models do not include production of Na via proton captures.

Finally we find that, in spite of the fact that the mixing scheme strongly affects the proton-ingestion episodes, our results for the  $s$  process are qualitatively the same as the results presented by Cristallo et al. (2009a) for a  $1.5 M_{\odot}$  star of metallicity half of that used in our models ( $Z = 5 \times 10^{-5}$ ) which also experience a proton-ingestion episode. From Fig. 6 of Cristallo et al. (2009a) we see that after the first TDU episode, which records the effect of the proton-ingestion event, the  $s$  process favours the production of the lighter elements, just like our models. The final  $[\text{Ba}/\text{Sr}] \simeq 0.40$ ,  $[\text{Ba}/\text{Eu}] \simeq 0.95$ , and  $[\text{Pb}/\text{Ba}] \simeq 0.85$  are close to those obtained in our  $1.25 M_{\odot}$  and  $1.5 M_{\odot}$  models.

## 4. Comparison with the abundances of CEMP-*s* and CEMP-*s/r* stars

### 4.1. [Ba/Fe] versus [Eu/Fe]

Figure 5 presents an overview of the observational data for CEMP stars and carbon-normal metal-poor stars of the *rI* and *rII* subclasses following the data and classification of Masseron et al. (2010). In this and all the following figures we used different symbols for stars in different metallicity ranges, as indicated in the caption. There are no noticeable differences in the distribution of any of the plotted abundances when changing the metallicity, the only noticeable properties being that there are more CEMP-*s* than CEMP-*s/r* stars with  $[\text{Fe}/\text{H}] > -2$ , and more CEMP-no stars with  $[\text{Fe}/\text{H}] < -3$  than in the other CEMP star classes. The different classes of CEMP stars appear to be fairly well distinguished in this plot. Most of the CEMP-no Eu data are upper limits, and the only CEMP-*rII* star, CS 22892-052, appears indistinguishable from the rest of the *rII* group in terms of its heavy element composition.

The two groups of CEMP-*s* and CEMP-*s/r* appear to be distinct, with CEMP-*s/r* having higher [Eu/Fe] ratio in absolute terms, but also higher [Ba/Fe] on average. In Fig. 5 we plot the correlation lines of the two groups. The similar slope, around 1, indicates that for both classes the linear dependence would be preserved in a non-logarithmic scale. What counts here is the y-intercept, which corresponds to [Ba/Eu] and thus defines the slope of the linear correlation between the two variables in a non-logarithmic scale: in the case of CEMP-*s* stars the process responsible for their compositions produces on average of around 400 times more Ba than Eu, with a spread of a factor of about 2; in the case of CEMP-*s/r* stars, instead, the process responsible for their composition produces on average of around 200 times more Ba than Eu, with a spread of a factor of about 2. Not surprisingly, the *r* stars also sit on a correlation line with a slope of around 1 and y-intercept of around  $-0.6$ , corresponding to the solar-system *r*-process Ba/Eu ratio of about 10. In the case of CEMP-*s* the [Ba/Eu] value of  $+0.89$  agrees very well with the typical [Ba/Eu] ratios reported in Tables 3, 4, and 6, while in the case of CEMP-*s/r*, the value of  $+0.6$  does not agree with any AGB models producing  $[\text{Ba}/\text{Fe}] > 1$ .

The three CEMP-*s/r* with the lowest Ba abundance in their group may belong instead to the CEMP-*s* group. This seems likely for BS 16080-175, with  $[\text{Ba}/\text{Fe}] = 1.55$  and  $[\text{Eu}/\text{Fe}] = 1.05$ , which can be reclassified as CEMP-*s* within the 0.07 dex uncertainties. The other two outliers BS 17436-058, with  $[\text{Ba}/\text{Fe}] = 1.60$  and  $[\text{Eu}/\text{Fe}] = 1.17$ , and HD 187861, with  $[\text{Ba}/\text{Fe}] = 1.39$  and  $[\text{Eu}/\text{Fe}] = 1.34$ , may be reclassified as CEMP-*s* within  $2\sigma$  of their 0.11 and 0.20 dex [Eu/Fe] uncertainties. However, we note that  $[\text{La}/\text{Fe}] = 1.73 \pm 0.2$  in HD 187861 indicates that it should be re-classified as a CEMP-*s/r* star. More observations and analysis

of these stars will help to clarify their status.

Another interesting case is that of CS 30322-023 ( $[\text{Ba}/\text{Fe}]=0.52$  and  $[\text{Eu}/\text{Fe}]=-0.63$ ), which has been previously classified as a CEMP-*s* (Aoki et al. 2007), and was included in the CEMP-low-*s* class by Masseron et al. (2010). This star has the highest  $[\text{N}/\text{C}] \simeq +2$  and the lowest, and only negative,  $[\text{Eu}/\text{Fe}]$  ratio in the sample, as well as  $[\text{Fe}/\text{H}] \simeq -3.3$ , at the lower end of the CEMP-*s* range. Another three stars have  $[\text{N}/\text{C}] > 1$ : CS 22949-037, CS 22960-053, and CS 29528-041, which all have  $[\text{Fe}/\text{H}]$  similar to CS 30322-023 and are classified as CEMP-no by Masseron et al. (2010). However, CS 22960-053 and CS 29528-041 have  $[\text{Ba}/\text{Fe}] \simeq 0.9$  but no Eu observations, so they may belong to the CEMP-low-*s* class (as defined by Masseron et al. 2010), together with CS 30322-023. In fact, Aoki et al. (2007) classified both CS 22960-053 and CS 30322-023 as CEMP-*s* stars following Ryan et al. (2005).

Figure 6 includes a selection of our model predictions together with the data of Fig. 5. In this as in all the following figures the solid lines are a visual aid connecting the predicted envelope composition after each TDU episode. These prediction lines are not straight because the composition of the *s*-process material in the He intershell evolves with time and because the variables are shown on a logarithmic scale. The process of transferring and mixing AGB material onto the companion star would result in mixing lines connecting the AGB composition with the initial composition. These mixing lines closely follow the plotted AGB evolution lines and are not shown in the figure. We include in the figure the same stellar models plotted in Figs. 2 and 3, representing cases where the neutron-capture nucleosynthesis occurs in the different regimes described in § 3. All the plotted models start from a solar composition,  $[\text{Ba}/\text{Fe}]=[\text{Eu}/\text{Fe}]=0$ , except for the three  $2 M_{\odot}$  models from the Stromlo set with different initial composition:  $[r/\text{Fe}]=+0.4$ ,  $[r/\text{Fe}]=+1.0$ , and  $[r/\text{Fe}]=+2.0$  included in the lower panel of Fig. 6.

All the models produce both Ba and Eu. The predictions lines follow the trend of the CEMP-*s* group. A small spread in the initial *r*-process composition up to  $[r/\text{Fe}]=\pm 0.4$  dex, which is within the composition observed in field stars of the corresponding metallicity (see, e.g., Fig. 2 of Bisterzo et al. 2011b), is enough to cover the data. CS 30322-023 indicates an initial negative  $[r/\text{Fe}] \approx -0.6$ , which would also be within the observed range at the corresponding metallicity  $[\text{Fe}/\text{H}]=-3.3$ . On the other hand, AGB models do not produce the high  $[\text{Eu}/\text{Fe}]$  observed in CEMP-*s/r* stars.

One solution to this problem may be to increase the initial  $[r/\text{Fe}]$  abundance by up to +2 dex under the assumption that the *r*-process enrichment is primordial in these systems (bottom panel of Fig. 6). This primordial enrichment can arise by assuming that the molecular clouds where CEMP-*s/r* stars formed were polluted by *r*-process elements from a

nearby SNII. This scenario provides a solution for the highest measured [Eu/Fe] abundances in CEMP-*s/r* stars as discussed in detail by Bisterzo et al. (2011b). However, it comes with three problems, some of which have been discussed previously (see e.g. Jonsell et al. 2006; Lugaro et al. 2009). (1) The initial [r/Fe] value does not affect the final [Ba/Fe] value, which remains constant, hence the linear correlation observed between the Eu and Ba enhancements in the CEMP-*s/r* sample is not reproduced. (2) The number of *r*II stars (around 10) is smaller than the number of CEMP-*s/r* stars (about 30), so, it seems unlikely that CEMP-*s/r* stars evolved from *r*II stars in binary systems, because these should make up a fraction of all *r*II stars. This does not appear to be an observational bias since stellar surveys such as the Hamburg/ESO R-process-Enhanced Stars (HERES) have specifically targeted *r*I and *r*II stars. It is also difficult to invoke supernova triggering as the cause for the formation of binaries: though early work indicated this link possible (Vanhala & Cameron 1998), it is now understood that formation of binaries occurs very naturally whenever a turbulent velocity field is present in a molecular cloud (Bate 2009). Furthermore the whole concept of supernova-triggered star formation is still controversial, both observationally and theoretically (Leão et al. 2009; Elmegreen 2011). (3) The metallicity distribution is different for the two samples: [Fe/H] is centered at  $\simeq -2.5$  for CEMP-*s/r* stars and at  $\simeq -2.8$  for *r*II stars.

#### 4.2. [ls/hs] versus [Mg/hs]

In this and the following subsections we compare our model predictions to the observations using “intrinsic” indicators, i.e., elemental ratios that include only elements that are produced in AGB stars. Different from the [Ba/Fe] and [Eu/Fe] ratios considered above, where Fe is not produced in AGB models, the “intrinsic” ratios move away from their initial solar values towards their *s*-process values already after a small number of TPs (though this is less true for the  $5 M_{\odot}$  model where the dilution in the envelope is much larger than in the other models). For the CEMP stars, this means that the intrinsic ratios are close to the AGB values even for relatively large dilutions of the AGB material onto the CEMP star. Hence, intrinsic ratios are, in a first approximation, independent of the TDU, the mass loss, the stellar lifetime, and the accretion and mixing processes on the binary companion. Instead, they mostly constrain the nucleosynthesis occurring in the deep layers of the star and in our context, the neutron source and the neutron flux for the *s* process.

We also note that we consider here ratios of elements that are all significantly produced in AGB stars, so that variations in the initial composition of these elements due to the chemical evolution of the Galaxy do not have a significant effect on the AGB predictions. Using the initial composition from Kobayashi et al. (2011) (i.e., [F/Fe], [Na/Fe], and [Mg/Fe]

equal to  $-1.5$ ,  $-0.2$ , and  $+0.3$  dex, respectively) did not lead to modifications of the results plotted and discussed here in selected models with mass  $\geq 1.5 M_{\odot}$ . Only the  $[\text{Mg}/\text{Fe}]$  ratio of stars with masses lower than  $1.5 M_{\odot}$  may be more strongly effected by the initial composition because these models experience less dredge-up. For these models, this effect would at most shift the  $[\text{Mg}/\text{hs}]$  ratios by  $+0.3$  dex.

Figure 7 shows the  $[\text{ls}/\text{hs}]$  and  $[\text{Mg}/\text{hs}]$  observed in CEMP-*s* and CEMP-*s/r* stars together with our model predictions. The dispersion of the data is quite large, however, it clearly shows the presence of a linear correlation with slope  $\simeq 1$ . The y-intercept  $\simeq 0$  indicates that this correlation is most likely due to variations in the amount of the hs elements, Ba, La, and Ce. As noted in previous studies (see, e.g., Fig. 9 and Fig. 6 of Jonsell et al. 2006; Bisterzo et al. 2011b, respectively), the CEMP-*s/r* stars are separated from the CEMP-*s* in that they show  $[\text{ls}/\text{hs}]$  lower by at least 0.5 dex. Here we show that CEMP-*s/r* stars also show lower  $[\text{Mg}/\text{hs}]$  than CEMP-*s*. It seems obvious to ascribe these differences to the fact that CEMP-*s/r* stars have, on average, higher hs abundances than CEMP-*s* (Fig. 6).

All our models produce  $[\text{ls}/\text{hs}] > -1$ . This derives from the basic way in which the *s* process operates (see also Busso et al. 2001). As the neutron flux increases, first the ls elements, then the hs elements, and finally Pb are produced. As the flux goes through these peaks the abundances reach their equilibrium values, above which it is not possible to increase them. This is similar to the situation of buckets connected to each other. When water is poured into the first bucket, the bucket fills up. Once it is full, the water starts moving into the second bucket and so on. The relative amount of water in the two buckets is only determined by their size (the neutron-capture cross sections in the case of the ls and hs elements) and not by how much more water is poured into the system<sup>7</sup>. Hence, the minimum  $[\text{ls}/\text{hs}]$  ratio is the value expected when the *s* process is in equilibrium through the first and the second *s*-process peaks (with  $\sigma_{\Lambda} N_{\Lambda} = \text{constant}$ ). This  $[\text{ls}/\text{hs}]$  ratio is roughly equal to  $-1$  because the neutron-capture cross section and the solar abundance of, e.g.,  $^{138}\text{Ba}$  are about 1.5 and 6 times lower (respectively) than those of, e.g.,  $^{88}\text{Sr}$ . On the other hand, the  $[\text{Pb}/\text{hs}]$  ratio cannot reach an equilibrium value because Pb is at the end of the *s*-process chain. The Pb abundance can continue to grow indefinitely as more neutrons are made available.

Unless we ascribe the overall mismatch to the large error bars, which still would not explain why CEMP-*s/r* stars are separated from CEMP-*s* stars in terms of both  $[\text{ls}/\text{hs}]$  and  $[\text{Mg}/\text{hs}]$ , it appears that a fraction of CEMP-*s/r* stars do not carry a typical pure *s*-process signature in the relative abundances of their *s*-process elements. Together with Fig. 6, Fig. 7

---

<sup>7</sup>To finish with this simile, we note that the third bucket, corresponding to the Pb peak in the *s* process, would have an infinite size.

demonstrates that (i) CEMP-*s/r* stars have the highest abundances of hs elements, and thus the lowest [ls/hs] and [Mg/hs] down to  $-2^8$ , and (ii) our *s*-process models can match the observations well for CEMP-*s* stars, but cannot match those of CEMP-*s/r* stars, not only in terms of their Eu abundance, but also in terms of their ls and hs abundances.

Focusing on the CEMP-*s* stars only, they appear to be overall better matched by the models with the  $^{13}\text{C}$  neutron source burning radiatively. The  $5 M_{\odot}$  model, which could not be ruled out as a match to the observations on the basis of the Ba and Eu enhancements (Fig. 6), produces too much Mg and ls with respect to hs to be able to match any of the CEMP-*s* and CEMP-*s/r* data. Inspection of the results for the  $5.5 M_{\odot}$  model in Table 4 shows that inclusion of the  $^{13}\text{C}$  pocket does not solve this problem. On the other hand, the composition of CS 30322-023, the only CEMP-*s* with [Mg/hs]>0, is compatible with the models of  $3 M_{\odot}$  and  $5.5 M_{\odot}$  computed with the inclusion of the  $^{13}\text{C}$  pocket.

### 4.3. [Pb/hs] versus [Mg/hs]

Figure 8 presents the [Pb/hs] and [Mg/hs] observed in CEMP-*s* and CEMP-*s/r* stars together with our model predictions. The dispersion of the data is large and there is no obvious correlation between the two ratios. While the two classes are different in all the other abundance ratios considered so far, the distribution of [Pb/hs] in CEMP-*s* and CEMP-*s/r* stars covers the same range. The models with the  $^{13}\text{C}$  neutron source burning radiatively provide a good match to CEMP-*s* stars, where the spread in the [Pb/hs] ratio can be explained by varying the TDU number or, equivalently, the initial stellar mass (see also Bonačić Marinović et al. 2007). The models where the  $^{13}\text{C}$  neutron source burns convectively can provide a match for the lower end of the [Pb/hs] ratios observed in CEMP-*s/r* stars, however, as shown in the previous section, they do not match the [ls/hs] values of CEMP-*s/r*. Even though the error bars are large, CEMP-*s/r* stars with high [Pb/hs] ratios are not matched by any models.

We note that the  $5 M_{\odot}$  model does not cover any of the data points. As in the case of the [ls/hs] versus [Mg/hs] the composition of CS 30322-023 can be matched by intermediate-mass AGB models (e.g.,  $3 M_{\odot}$  and  $5.5 M_{\odot}$ ) if a  $^{13}\text{C}$  pocket is included.

---

<sup>8</sup>Specifically, the CEMP-*s/r* star with [ls/hs] $\simeq -2$  is HE 0212-0557 observed by Cohen et al. (2006). The hs value of this stars is based on values of [Ba/Fe], [Ce/Fe], and [La/Fe] all very similar to each other, while ls is based on [Y/Fe]=0.55, derived from three lines, and [Sr/Fe]=-0.05, derived from one line. Removing Sr from the calculation of ls still results in a very low [ls/hs]=-1.69.



#### 4.4. [ls/hs] and [Pb/hs] versus [Na/hs] and [F/hs]

Figures 9 and 10 present the [Na/hs] and [F/hs] ratios plotted versus the intrinsic  $s$ -process indicators, [ls/hs] and [Pb/hs]. There are not enough data to be able to determine if CEMP- $s$  and CEMP- $s/r$  stars are distinguished in their [Na/hs] and [F/hs] abundance ratios. The models where the  $^{13}\text{C}$  neutron source burns radiatively, which provide a good match to the overall composition of CEMP- $s$  stars in terms of their [Mg/hs], [ls/hs], and [Pb/hs] compositions, typically produce too much Na and F with respect to the hs elements to match any of the observational data. One exception is the case of CS 30322-023, the only CEMP- $s$  with [Na/hs]>0: this star is again distinguished from the rest of the CEMP- $s$  stars and as mentioned above may carry the signature of a more massive AGB star. A better overall match to [Na/hs] and [F/hs] is provided by the low-mass Stromlo models where the  $^{13}\text{C}$  neutron source burns convectively, however, these models do not cover the corresponding [Pb/hs] (and [ls/hs]) ratios.

As discussed in § 3.1 the predicted abundance of Na is made by both neutron and proton captures on  $^{22}\text{Ne}$ . The fraction made by neutron captures is linked to the production of Mg, and the models where the  $^{13}\text{C}$  neutron source burns radiatively provide a good match to the [Mg/hs] observed in CEMP- $s$ . The fraction made via proton captures, on the other hand, is disconnected from the production of Mg, but depends on the details of the proton-ingestion episodes, the profile of protons introduced to make the  $^{13}\text{C}$  pocket, and the proton-capture reaction rates of  $^{22}\text{Ne}$  and  $^{23}\text{Na}$  (which are uncertain, see Iliadis et al. 2010). All these uncertainties need to be tested to see if it is possible to match the observed [Na/hs] and [Mg/hs] ratios, which indicate that the production of Na via proton captures should be minimised. During the proton diffusion leading to the formation of the  $^{13}\text{C}$  pocket, a proton profile weighed towards a low proton abundance (e.g., the “fast” profile in Fig. 10 of Goriely & Mowlavi 2000) may contribute to the solution of this problem. This possibility will be investigated in detail in a forthcoming study and has the potential to provide a strong constraint on the formation of the  $^{13}\text{C}$  pocket. A lower value of the  $^{22}\text{Ne}(p,\gamma)^{23}\text{Na}$  reaction rate or a higher value of the  $^{23}\text{Na}(p,\alpha)^{20}\text{Ne}$  reaction rate could also help lower the predicted Na abundances.

The predicted [F/hs] ratios are also higher than the observed upper limits. The operation of some form of deep mixing of the envelope material of the AGB companion star down to regions where H burning occurs, which is also invoked to explain the observed high N enhancements and low  $^{12}\text{C}/^{13}\text{C}$  ratios (see, e.g., Stancliffe 2010) may contribute to decreasing the F abundance in these stars. Further investigations are required to test this idea. Note that in the  $5 M_{\odot}$  model with HBB, F is strongly depleted by proton captures.

## 5. Summary and conclusions

We have presented a large set of stellar models at metallicity  $[\text{Fe}/\text{H}]=-2.3$  from two different evolutionary codes for which we have computed detailed  $s$ -process nucleosynthesis. For the first time we have presented abundance predictions for the elements heavier than iron from stars with masses lower than  $1.3 M_{\odot}$  and above  $2 M_{\odot}$  at this metallicity. The most up-to-date models including the effect of molecular opacities that vary with the envelope composition during the AGB evolution experience less TPs, less TDU episodes, and produce overall lower enhancements of the  $s$ -process elements with respect to Fe.

We have found that there are four regimes of neutron-capture processes and the dominant regime depends on the initial stellar mass: for the highest mass models the  $^{22}\text{Ne}$  neutron source is dominant and the inclusion of a  $^{13}\text{C}$  pocket where  $^{13}\text{C}$  burns radiatively has an effect only on the production of Pb; for models of mass  $< 3.5 M_{\odot}$ ,  $^{13}\text{C}$  is the main neutron source. For masses  $\simeq 2 M_{\odot}$ ,  $^{13}\text{C}$  burns radiatively in the  $^{13}\text{C}$  pocket during the interpulse periods. For lower masses,  $^{13}\text{C}$  also burns convectively as the first few  $^{13}\text{C}$  pocket are engulfed in the following TPs before  $^{13}\text{C}$  is completely burnt in the interpulse period. For the lowest masses, proton-ingestion episodes associated with the first few TPs also produce  $^{13}\text{C}$ , which burns convectively inside the TPs. Neutrons released during convective TPs produce lower  $[\text{Pb}/\text{hs}]$  ratios than neutrons released in the  $^{13}\text{C}$  pocket under radiative conditions, and higher  $[\text{ls}/\text{hs}]$  ratios if a smaller number of protons are ingested. It should be kept in mind that proton ingestion episodes are extremely sensitive to the convective mixing scheme adopted. Our models provide some insight into the effect of these episodes on the  $s$ -process distribution, and are in agreement with the results presented by Cristallo et al. (2009a). However, more detailed 3D models of the kind presented by Stancliffe et al. (2011) are needed to accurately ascertain the effect of proton-ingestion episodes on the  $s$ -process in AGB stars. The production of Mg and Na increases with the stellar mass as there is more primary  $^{22}\text{Ne}$  seed available.

From comparison with the observational data-set of CEMP stars compiled by Masseron et al. (2010) we have derived that our AGB models, especially those with radiative  $^{13}\text{C}$  burning, present a very good match to the composition of CEMP- $s$  stars. On the other hand, they cannot match the compositions of CEMP- $s/r$  stars, since they cannot produce the observed Eu enhancements up to one order of magnitude higher than in CEMP- $s$  stars. If the  $s$  process and  $r$  process components, making Ba and Eu, respectively, in CEMP- $s/r$  stars are completely independent, as in the scenario where the  $r$  enrichment is primordial, it is difficult to explain why the observed Ba and Eu are correlated. This is because for any given initial  $[r/\text{Fe}]$  abundance pattern imposed, the AGB models produce the same final  $[\text{Ba}/\text{Fe}]$  abundance. Since this conclusion relies on the observed correlation between Ba and Eu,

it is urgent to confirm and establish this correlation using a larger number of CEMP- $s/r$  star abundances derived from high-resolution spectroscopy and for a larger number of hs elements.

Not only do CEMP- $s/r$  and CEMP- $s$  stars differ in that CEMP- $s/r$  stars have more Eu than CEMP- $s$  stars in absolute terms, but they also differ in that CEMP- $s/r$  stars have on average more Ba (and other hs elements) than CEMP- $s$  stars. This behaviour is not readily explained if the  $s$ -process component in CEMP- $s$  and CEMP- $s/r$  stars come from the same AGB star sources. Furthermore, the higher Ba (hs) abundances are not accompanied by higher abundances in Mg and in the ls elements, as it is expected in our models. In fact, our AGB models always produce  $[ls/hs] > -1$ , which is too high to match the distribution of the  $s$ -process elements in CEMP- $s/r$  with  $[ls/hs]$  down to  $\simeq -2$ . On the other hand the higher Ba abundances are accompanied by higher Pb abundances, as expected in the  $s$  process. In summary, the composition of CEMP- $s/r$  stars is characterised by large enhancements of the hs elements and of Eu (correlated with Ba:  $\simeq 1/200$  Ba), as well as of Pb, but not of the ls elements. It remains to be seen if these compositions could be achieved by a “ $s/r$ ” neutron-capture process, which may be a single neutron-capture process with features in-between or a superposition of the  $s$  and  $r$  processes. Parametric models of neutron-capture processes will be a first step in establishing if this is a possibility.

If the Ba versus Eu correlation in CEMP- $s/r$  stars is confirmed and if it is not due to a new “ $s/r$ ” neutron-capture process, but to the  $s$  process and the  $r$  processes occurring in AGB stars and SNIe, respectively, then these sites must be somehow correlated to each other. A probably unlikely scenario, which we provide here as an illustrative example, is that of a stable triple stellar system comprising the CEMP- $s/r$  star observed today, a former AGB star, and a former SNII. In this case the orbital parameters such as the distance between the stars, which affect the mass transfer, are correlated, probably resulting in correlated Ba and Eu abundances.

While the AGB models produce a good match to the observed  $[Mg/hs]$  ratios in CEMP- $s$  stars, they typically produce too high  $[Na/hs]$  and  $[F/hs]$  ratios. This may depend on the choice of the proton profile leading to the formation of the  $^{13}C$  pocket, the proton-capture reaction rates involved, and the occurrence of extra-mixing processes. Investigation of these issues may result in important constraints on these uncertain stellar and nuclear inputs.

Finally, CS 30322-023 may carry the signature of nucleosynthesis in intermediate-mass AGB stars. This would be difficult to reconcile with the suggestion of Masseron et al. (2006) that this star is an intrinsic AGB object based on the low  $\log g = -0.3$ . This would make this star an extremely peculiar object born less than a half a Gyr ago, but with an extremely low metallicity typical of the early Universe. Our conclusions are more in line with the

higher value of  $\log g = 1$  reported by Aoki et al. (2007), not indicative of an intrinsic AGB star. From the preliminary comparison made here the composition of CS 30322-023 indicates that both HBB and the  $^{13}\text{C}$  pocket were operating in low-metallicity massive AGB stars. However, before drawing conclusions we need to compare the composition of this star with predictions from a model of the appropriate metallicity of  $[\text{Fe}/\text{H}]=-3.3$ . Observations of Eu in CS 22960-053 and CS 29528-041 may reveal that these two stars are also CEMP-low- $s$  with  $[\text{N}/\text{C}]>1$  creating a new class together with CS 30322-023. Future studies will focus on comparison of single stellar objects with our AGB model predictions.

We heartily thank Sara Bisterzo for lengthy and thorough discussion and extensive criticism, which have led to major improvements of this paper and for help in setting up Table 6. We thank Thomas Masseron for help on the observational data points and Daniel Price for discussion on star formation. We also thank the anonymous referee for helping to improve the discussion and clarity of the presented results. ML and AIK are grateful for the support of the NCI National Facility at the ANU. ML is an ARC Future Fellow and Monash Research Fellow. AIK is a Stromlo Fellow. RJS is a Stromlo Fellow and acknowledges support from the Australian Research Council’s Discovery Projects funding scheme (project number DP0879472) during his time at Monash University.

## REFERENCES

- Abia, C., Busso, M., Gallino, R., Domínguez, I., Straniero, O., & Isern, J. 2001, *ApJ*, 559, 1117
- Angulo, C., Arnould, M., Rayet, M., Descouvemont, P., Baye, D., Leclercq-Willain, C., Coc, A., Barhoumi, S., Aguer, P., Rolfs, C., Kunz, R., Hammer, J. W., Mayer, A., Paradellis, T., Kossionides, S., Chronidou, C., Spyrou, K., degl’Innocenti, S., Fiorentini, G., Ricci, B., Zavatarelli, S., Providencia, C., Wolters, H., Soares, J., Grama, C., Rahighi, J., Shotton, A., & Laméhi Rachti, M. 1999, *Nucl. Phys. A*, 656, 3
- Aoki, W., Beers, T. C., Christlieb, N., Norris, J. E., Ryan, S. G., & Tsangarides, S. 2007, *ApJ*, 655, 492
- Arlandini, C., Käppeler, F., Wisshak, K., Gallino, R., Lugaro, M., Busso, M., & Straniero, O. 1999, *ApJ*, 525, 886
- Asplund, M., Grevesse, N., Sauval, A. J., & Scott, P. 2009, *ARA&A*, 47, 481

- Bate, M. R. 2009, *MNRAS*, 392, 590
- Beers, T. C. & Christlieb, N. 2005, *ARA&A*, 43, 531
- Bemmerer, D., Confortola, F., Lemut, A., Bonetti, R., Brogini, C., Corvisiero, P., Costantini, H., Cruz, J., Formicola, A., Fülöp, Z., Gervino, G., Guglielmetti, A., & Gustavino, C. 2006, *Nuclear Physics A*, 779, 297
- Bessell, M. S., Brett, J. M., Wood, P. R., & Scholz, M. 1989, *A&AS*, 77, 1
- Bisterzo, S., Gallino, R., Straniero, O., Cristallo, S., & Käppeler, F. 2010, *MNRAS*, 404, 1529
- . 2011a, *MNRAS*, submitted
- . 2011b, *MNRAS* arXiv:1108.0500, 1716
- Bonačić Marinović, A., Izzard, R. G., Lugaro, M., & Pols, O. R. 2007, *A&A*, 469, 1013
- Boothroyd, A. I., Sackmann, I.-J., & Ahern, S. C. 1993, *ApJ*, 416, 762
- Busso, M., Gallino, R., Lambert, D. L., Travaglio, C., & Smith, V. V. 2001, *ApJ*, 557, 802
- Busso, M., Gallino, R., & Wasserburg, G. J. 1999, *ARA&A*, 37, 239
- Cameron, A. G. W. 1955, *ApJ*, 121, 144
- Campbell, S. W. & Lattanzio, J. C. 2008, *A&A*, 490, 769
- Cannon, R. C. 1993, *MNRAS*, 263, 817
- Carollo, D., Beers, T. C., Bovy, J., Sivarani, T., Norris, J. E., Freeman, K. C., Aoki, W., Lee, Y. S., & Kennedy, C. R. 2011, *ApJ* arXiv: 1103.3067
- Carollo, D., Beers, T. C., Lee, Y. S., Chiba, M., Norris, J. E., Wilhelm, R., Sivarani, T., Marsteller, B., Munn, J. A., Bailer-Jones, C. A. L., Fiorentin, P. R., & York, D. G. 2007, *Nature*, 450, 1020
- Chiosi, C., Wood, P. R., & Capitanio, N. 1993, *ApJS*, 86, 541
- Clayton, D. D. 1988, *MNRAS*, 234, 1
- Cohen, J. G., McWilliam, A., Sheckman, S., Thompson, I., Christlieb, N., Melendez, J., Ramirez, S., Swenson, A., & Zickgraf, F.-J. 2006, *AJ*, 132, 137

- Cohen, J. G., Shectman, S., Thompson, I., McWilliam, A., Christlieb, N., Melendez, J., Zickgraf, F., Ramírez, S., & Swenson, A. 2005, *ApJ*, 633, L109
- Cristallo, S., Piersanti, L., Straniero, O., Gallino, R., Domínguez, I., & Käppeler, F. 2009a, *PASA*, 26, 139
- Cristallo, S., Straniero, O., Gallino, R., Piersanti, L., Domínguez, I., & Lederer, M. T. 2009b, *ApJ*, 696, 797
- Denissenkov, P. A. & Tout, C. A. 2003, *MNRAS*, 340, 722
- Eggleton, P. P. 1971, *MNRAS*, 151, 351
- . 1972, *MNRAS*, 156, 361
- Eldridge, J. J. & Tout, C. A. 2004, *MNRAS*, 348, 201
- Elmegreen, B. G. 2011, *Ecole Evry Schatzman 2010: Star Formation in the Local Universe*, arXiv:1101.3112
- Ferguson, J. W., Alexander, D. R., Allard, F., Barman, T., Bodnarik, J. G., Hauschildt, P. H., Heffner-Wong, A., & Tamanai, A. 2005, *ApJ*, 623, 585
- Frost, C. A. & Lattanzio, J. C. 1996, *ApJ*, 473, 383
- Gallino, R., Arlandini, C., Busso, M., Lugaro, M., Travaglio, C., Straniero, O., Chieffi, A., & Limongi, M. 1998, *ApJ*, 497, 388
- Goriely, S. & Mowlavi, N. 2000, *A&A*, 362, 599
- Goriely, S. & Siess, L. 2004, *A&A*, 421, L25
- Goriely, S. & Siess, L. 2005, in *IAU Symposium, Vol. 228, From Lithium to Uranium: Elemental Tracers of Early Cosmic Evolution*, ed. V. Hill, P. François, & F. Primas, 451–460
- Heil, M., Detwiler, R., Azuma, R. E., Couture, A., Daly, J., Görres, J., Käppeler, F., Reifarth, R., Tischhauser, P., Ugalde, C., & Wiescher, M. 2008, *Phys. Rev. C*, 78, 025803
- Herwig, F. 2000, *A&A*, 360, 952
- . 2004a, *ApJ*, 605, 425
- . 2004b, *ApJS*, 155, 651

- . 2005, *ARA&A*, 43, 435
- Hollowell, D. & Iben, Jr., I. 1988, *ApJ*, 333, L25
- Iglesias, C. A. & Rogers, F. J. 1996, *ApJ*, 464, 943
- Iliadis, C., Longland, R., Champagne, A. E., & Coc, A. 2010, *Nuclear Physics A*, 841, 323
- Iwamoto, N., Kajino, T., Mathews, G. J., Fujimoto, M. Y., & Aoki, W. 2004, *ApJ*, 602, 377
- Jonsell, K., Barklem, P. S., Gustafsson, B., Christlieb, N., Hill, V., Beers, T. C., & Holmberg, J. 2006, *A&A*, 451, 651
- Karakas, A. & Lattanzio, J. C. 2007, *PASA*, 24, 103
- Karakas, A. I. 2010, *MNRAS*, 403, 1413
- Karakas, A. I. & Lattanzio, J. C. 2003, *Publ. Astron. Soc. Aust.*, 20, 279
- Karakas, A. I., Lattanzio, J. C., & Pols, O. R. 2002, *Publ. Astron. Soc. Aust.*, 19, 515
- Karakas, A. I., Lugaro, M., Wiescher, M., Goerres, J., & Ugalde, C. 2006, *ApJ*, 643, 471
- Kobayashi, C., Karakas, A. I., & Umeda, H. 2011, *MNRAS*, 414, 3231
- Lattanzio, J. C. 1986, *ApJ*, 311, 708
- . 1991, *ApJS*, 76, 215
- Lau, H. H. B., Stancliffe, R. J., & Tout, C. A. 2009, *MNRAS*, 396, 1046
- Leão, M. R. M., de Gouveia Dal Pino, E. M., Falceta-Gonçalves, D., Melioli, C., & Gerassate, F. G. 2009, *MNRAS*, 394, 157
- Lederer, M. T. & Aringer, B. 2009, *A&A*, 494, 403
- Lucatello, S., Beers, T. C., Christlieb, N., Barklem, P. S., Rossi, S., Marsteller, B., Sivarani, T., & Lee, Y. S. 2006, *ApJ*, 652, L37
- Lucatello, S., Masseron, T., Johnson, J. A., Pignatari, M., & Herwig, F. 2011, *ApJ*, 729, 40
- Lucatello, S., Tsangarides, S., Beers, T. C., Carretta, E., Gratton, R. G., & Ryan, S. G. 2005, *ApJ*, 625, 825
- Lugaro, M., Campbell, S. W., & de Mink, S. E. 2009, *PASA*, 26, 322

- Lugaro, M., de Mink, S. E., Izzard, R. G., Campbell, S. W., Karakas, A. I., Cristallo, S., Pols, O. R., Lattanzio, J. C., Straniero, O., Gallino, R., & Beers, T. C. 2008, *A&A*, 484, L27
- Lugaro, M., Herwig, F., Lattanzio, J. C., Gallino, R., & Straniero, O. 2003, *ApJ*, 586, 1305
- Lugaro, M., Ugalde, C., Karakas, A. I., Görres, J., Wiescher, M., Lattanzio, J. C., & Cannon, R. C. 2004, *ApJ*, 615, 934
- Marigo, P. 2002, *A&A*, 387, 507
- Masseron, T., Johnson, J. A., Plez, B., van Eck, S., Primas, F., Goriely, S., & Jorissen, A. 2010, *A&A*, 509, A93+
- Masseron, T., van Eck, S., Famaey, B., Goriely, S., Plez, B., Siess, L., Beers, T. C., Primas, F., & Jorissen, A. 2006, *A&A*, 455, 1059
- Merrill, S. P. W. 1952, *ApJ*, 116, 21
- Montes, F., Beers, T. C., Cowan, J., Elliot, T., Farouqi, K., Gallino, R., Heil, M., Kratz, K., Pfeiffer, B., Pignatari, M., & Schatz, H. 2007, *ApJ*, 671, 1685
- Otsuka, M., Tajitsu, A., Hyung, S., & Izumiura, H. 2010, *ApJ*, 723, 658
- Pignatari, M., Gallino, R., Meynet, G., Hirschi, R., Herwig, F., & Wiescher, M. 2008, *ApJ*, 687, L95
- Pols, O. R., Tout, C. A., Eggleton, P. P., & Han, Z. 1995, *MNRAS*, 274, 964
- Reimers, D. 1975, *Circumstellar envelopes and mass loss of red giant stars (Problems in stellar atmospheres and envelopes.)*, 229–256
- Roberts, L. F., Woosley, S. E., & Hoffman, R. D. 2010, *ApJ*, 722, 954
- Ryan, S. G., Aoki, W., Norris, J. E., & Beers, T. C. 2005, *ApJ*, 635, 349
- Smith, V. V. & Lambert, D. L. 1986, *ApJ*, 311, 843
- Snedden, C., Cowan, J. J., & Gallino, R. 2008, *ARA&A*, 46, 241
- Snedden, C., Cowan, J. J., Lawler, J. E., Ivans, I. I., Burles, S., Beers, T. C., Primas, F., Hill, V., Truran, J. W., Fuller, G. M., Pfeiffer, B., & Kratz, K. 2003, *ApJ*, 591, 936
- Stancliffe, R. J. 2009, *MNRAS*, 394, 1051



- . 2010, MNRAS, 403, 505
- Stancliffe, R. J., Dearborn, D. S. P., Lattanzio, J. C., Heap, S. A., & Campbell, S. W. 2011, ApJ arXiv: 1109.1289
- Stancliffe, R. J. & Eldridge, J. J. 2009, MNRAS, 396, 1699
- Stancliffe, R. J. & Glebbeek, E. 2008, MNRAS, 389, 1828
- Stancliffe, R. J., Glebbeek, E., Izzard, R. G., & Pols, O. R. 2007, A&A, 464, L57
- Stancliffe, R. J., Lugaro, M., Ugalde, C., Tout, C. A., Görres, J., & Wiescher, M. 2005, MNRAS, 360, 375
- Stancliffe, R. J., Tout, C. A., & Pols, O. R. 2004, MNRAS, 352, 984
- Straniero, O., Gallino, R., Busso, M., Chieffi, A., Raiteri, C. M., Limongi, M., & Salaris, M. 1995, ApJ, 440, L85
- Suda, T. & Fujimoto, M. Y. 2010, MNRAS, 405, 177
- Suda, T., Katsuta, Y., Yamada, S., Suwa, T., Ishizuka, C., Komiya, Y., Sorai, K., Aikawa, M., & Fujimoto, M. Y. 2008, PASJ, 60, 1159
- Travaglio, C., Gallino, R., Arnone, E., Cowan, J., Jordan, F., & Sneden, C. 2004, ApJ, 601, 864
- Truran, J. W. & Iben, Jr., I. 1977, ApJ, 216, 797
- Van Eck, S., Goriely, S., Jorissen, A., & Plez, B. 2003, A&A, 404, 291
- van Raai, M., Lugaro, M., Karakas, A. I., García-Hernández, D. A., & Yong, D. 2011, A&A, submitted
- Vanhala, H. A. T. & Cameron, A. G. W. 1998, ApJ, 508, 291
- Vassiliadis, E. & Wood, P. R. 1993, ApJ, 413, 641
- Wallerstein, G. & Knapp, G. R. 1998, ARA&A, 36, 369

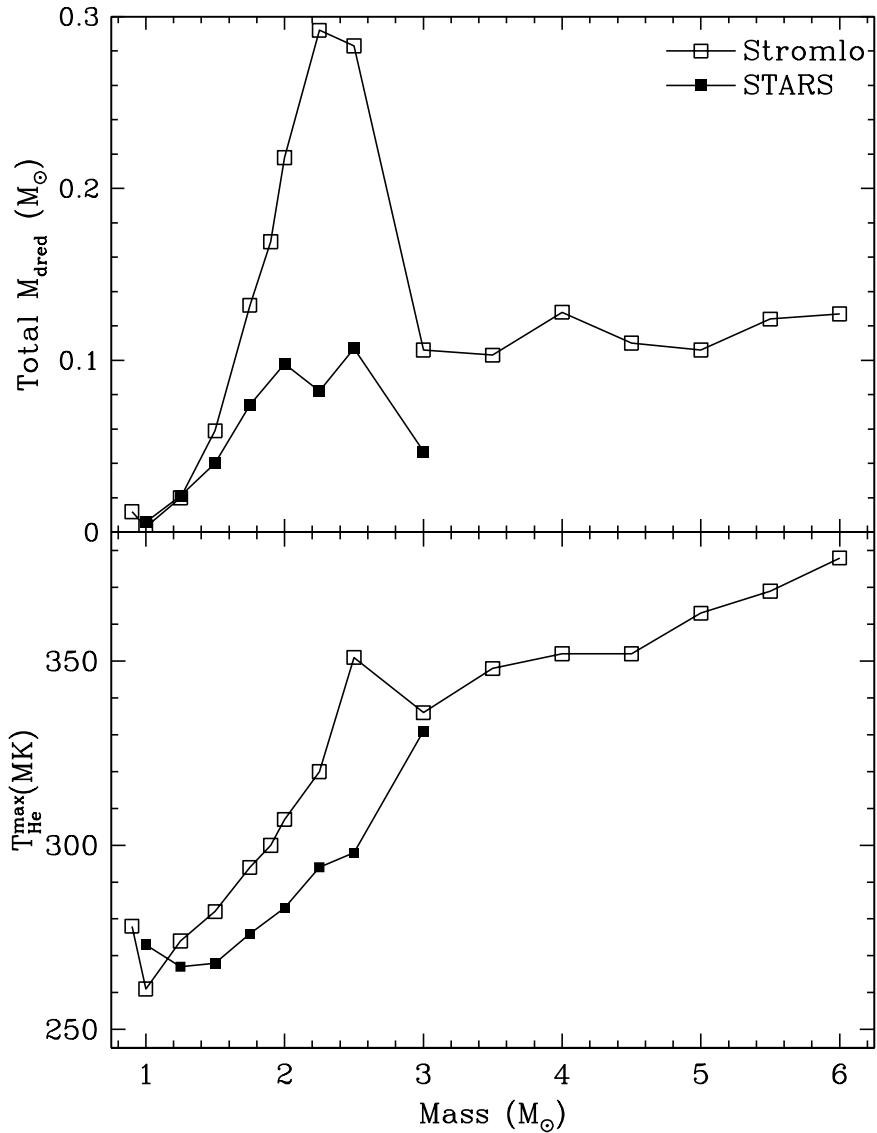


Fig. 1.— The total mass dredged-up by the TDU (top panel) and the maximum temperature at the base of TPs (bottom panel) as a function of the initial stellar mass for our AGB models. The change in the trend for the Stromlo models between  $2.5 M_{\odot}$  and  $3 M_{\odot}$  is caused by the change in the adopted mass-loss law (see the text for details). The use of the Reimers (1975) mass-loss prescription for stars with masses  $3 M_{\odot} - 6 M_{\odot}$  has the effect of shortening the AGB lifetime and reducing the number of TDU episodes.

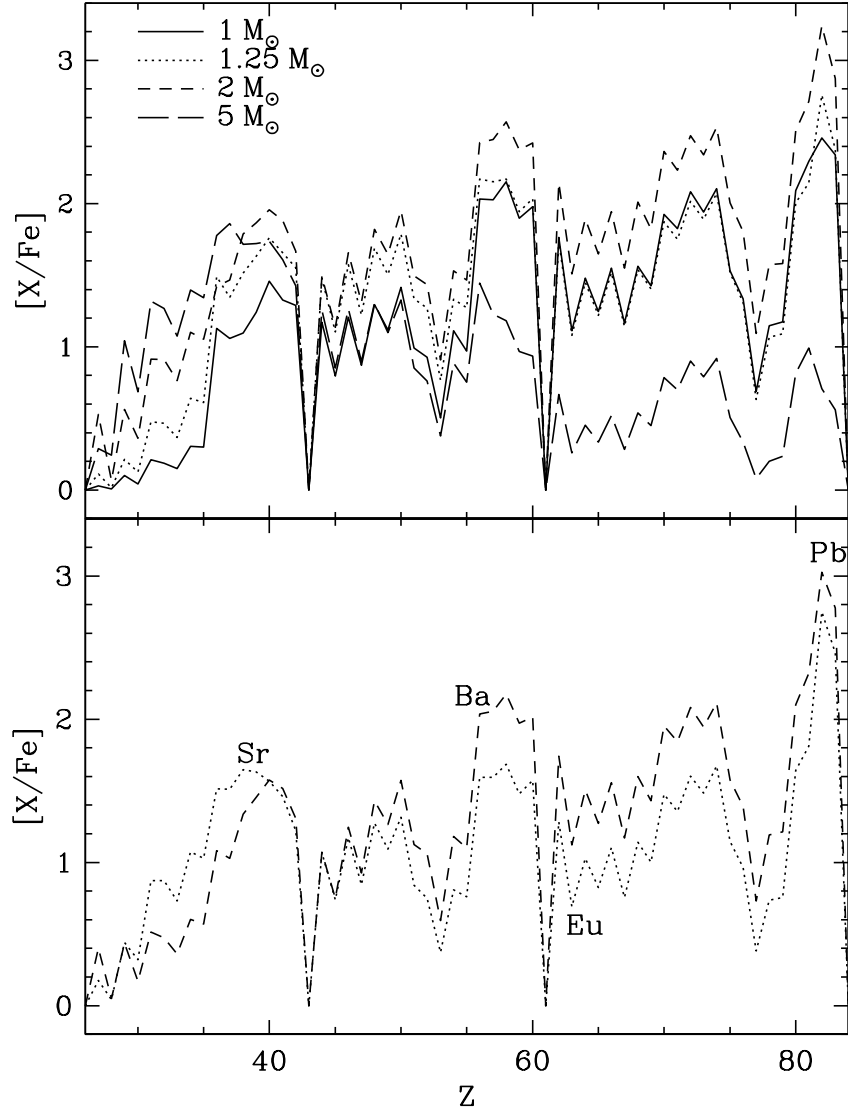


Fig. 2.— The  $[X/Fe]$  ratio as function of the atomic number  $Z$  for elements heavier than Fe for selected Stromlo (upper panel) and STARS (lower panel). Data are surface abundances after the last computed TP. The selected models represent cases where the neutron-capture nucleosynthesis occurs according to the four regimes: The  $5 M_{\odot}$  model represents the case where all neutrons are released by the  $^{22}\text{Ne}$  neutron source in the TPs (Regime 1). The  $2 M_{\odot}$  models represent the regime where most neutrons are released under radiative conditions during the interpulse periods by the  $^{13}\text{C}$  neutron source (Regime 2). The STARS  $1.25 M_{\odot}$  model represent a case where neutrons released in radiative conditions by the  $^{13}\text{C}$  neutron source primarily determine  $[Pb/Ba]$ , while  $[Ba/Sr]$  is also affected by  $^{13}\text{C}$  burning convectively (Regimes 2, 3, and 4). The Stromlo  $1.0 M_{\odot}$  and  $1.25 M_{\odot}$  models represent the regime where most of the neutrons are released in the convective TPs by the  $^{13}\text{C}$  neutron source (Regimes 3 and 4). All the other models show behaviour in between the selected models and are not included for the sake of clarity (all the data can be found in the on-line tables).

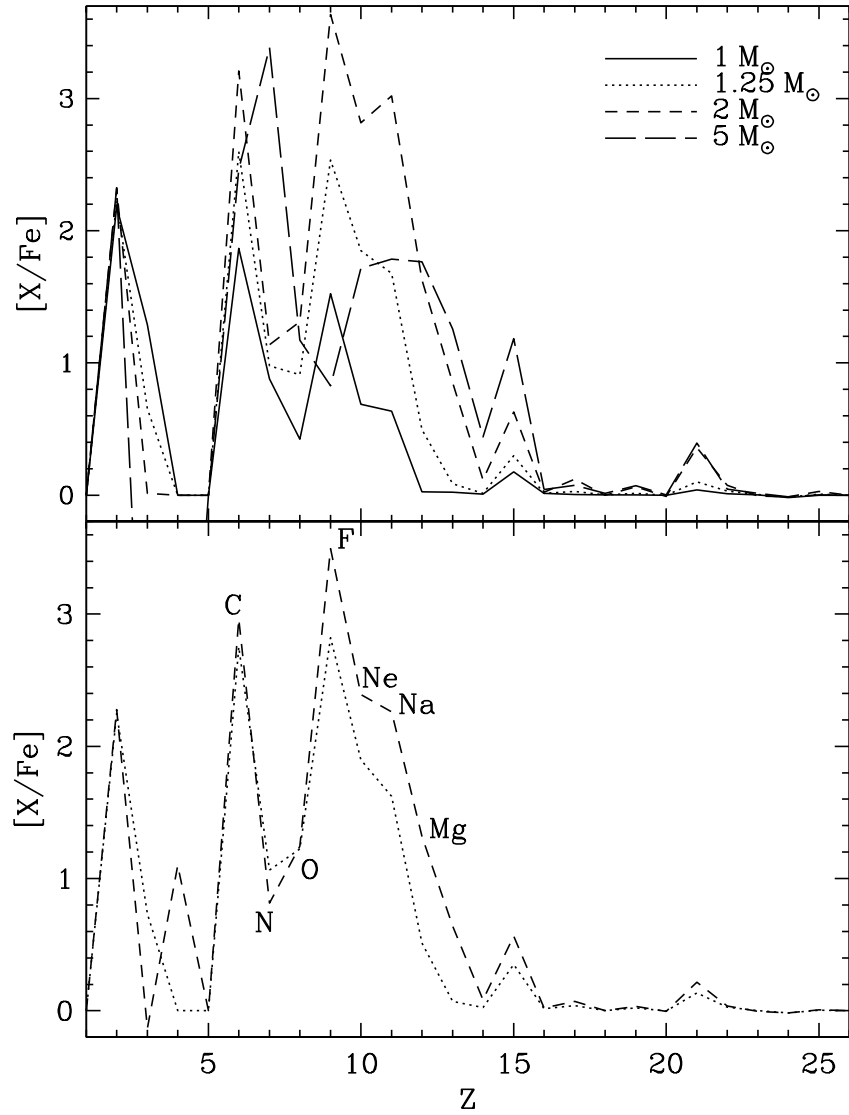


Fig. 3.— Same as Fig. 2 but showing the  $[X/Fe]$  ratios as a function of the atomic number  $Z$  for elements lighter than Fe. Stromlo models are shown in the upper panel and STARS models in the lower panel.

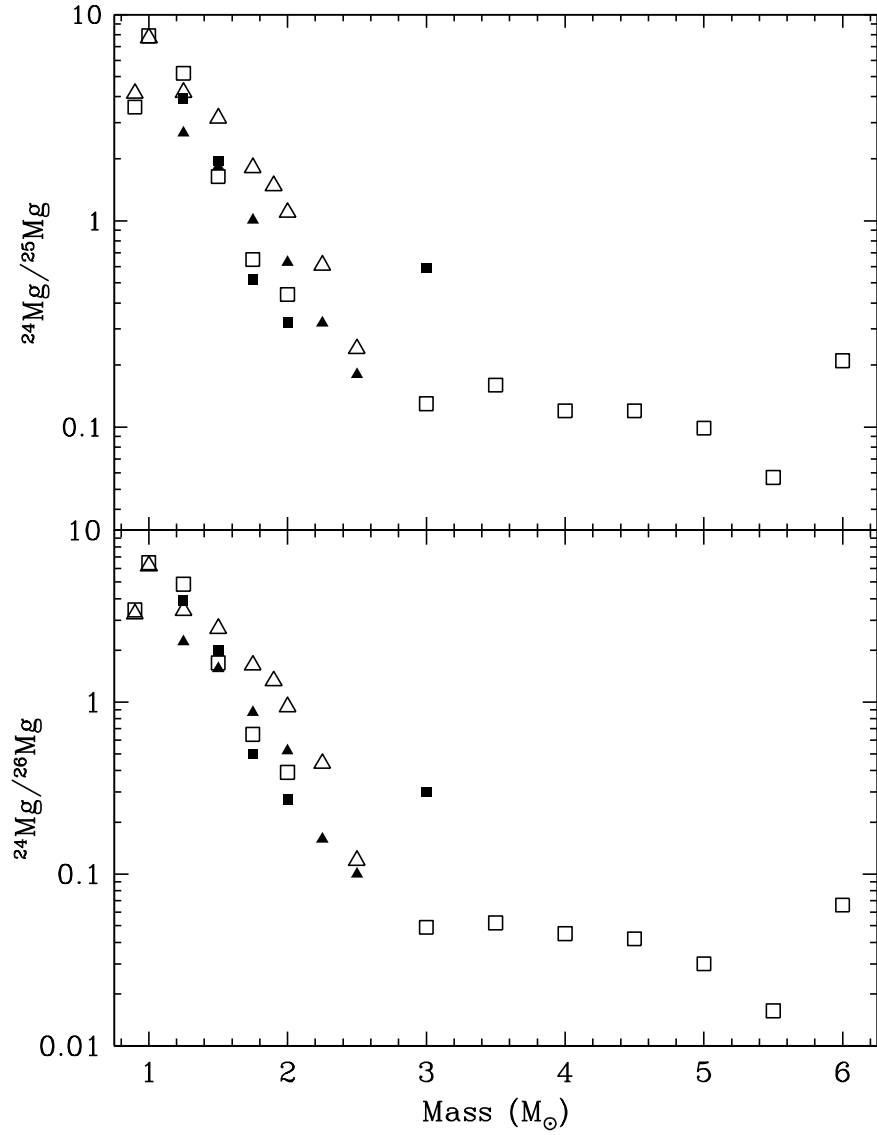


Fig. 4.— Mg isotopic ratios (by number) as function of the initial stellar mass: open symbols represent Stromlo models, black symbols represent STARS models. Squares are for models with  $M_{\text{mix}}=0$  and triangles are for models with  $M_{\text{mix}}=0.002 M_{\odot}$ .

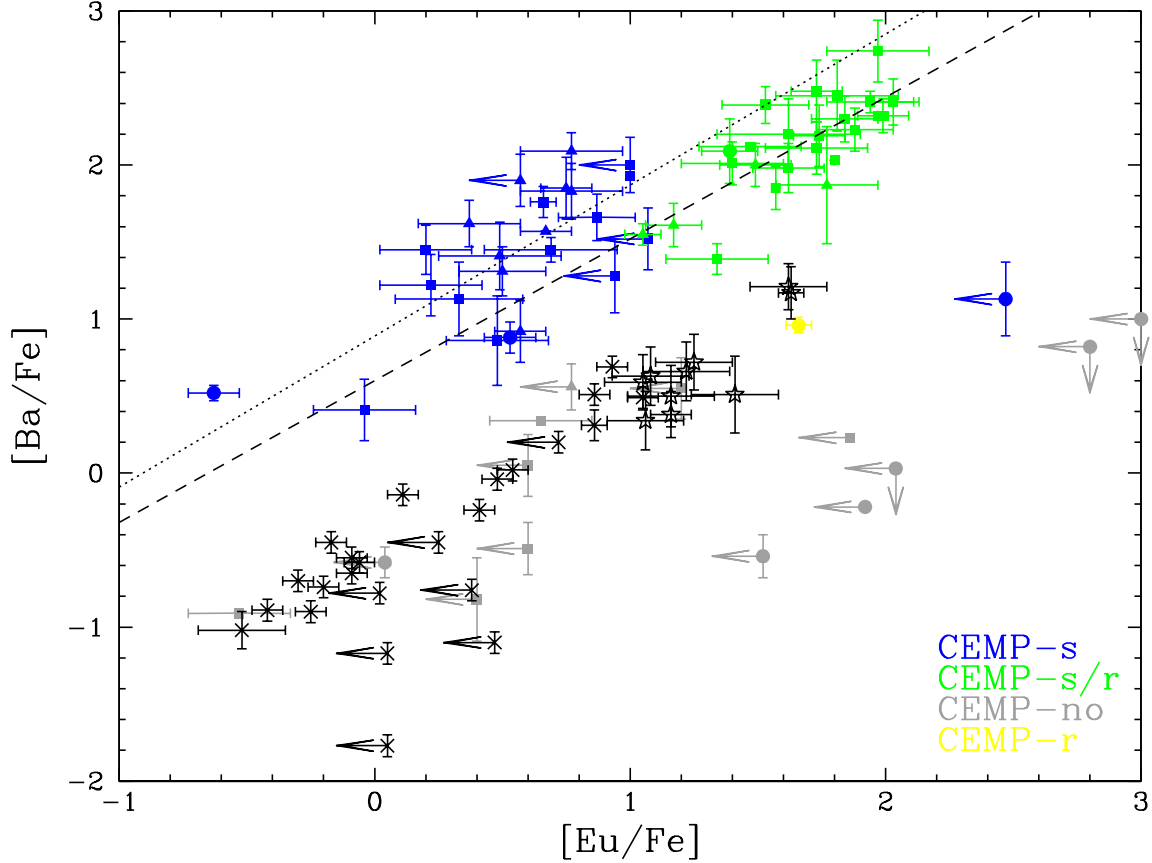


Fig. 5.— Overview of the observational data for CEMP stars (colour-coded as in the legend) and  $r$ I (black crosses) and  $r$ II (open star symbols) stars following the data and classification of Masseron et al. (2010) except that, for sake of simplicity, we have included the CEMP-low- $s$  in the CEMP- $s$  group. For CEMP stars, triangles represent stars with  $[\text{Fe}/\text{H}] > -2$ , squares represent stars with  $-3 < [\text{Fe}/\text{H}] < -2$ , and circles represent stars with  $[\text{Fe}/\text{H}] < -3$ . The correlation lines going through CEMP- $s$  (short-dashed line corresponding to  $[\text{Ba}/\text{Fe}] = 0.98 [\text{Eu}/\text{Fe}] + 0.89$ , with a correlation coefficient  $r=0.58$ ) and CEMP- $s/r$  (long-dashed line corresponding to  $[\text{Ba}/\text{Fe}] = 0.92 [\text{Eu}/\text{Fe}] + 0.60$ , with correlation coefficient  $r=0.59$ ) are also plotted. (A color version of this figure is available in the online journal.)

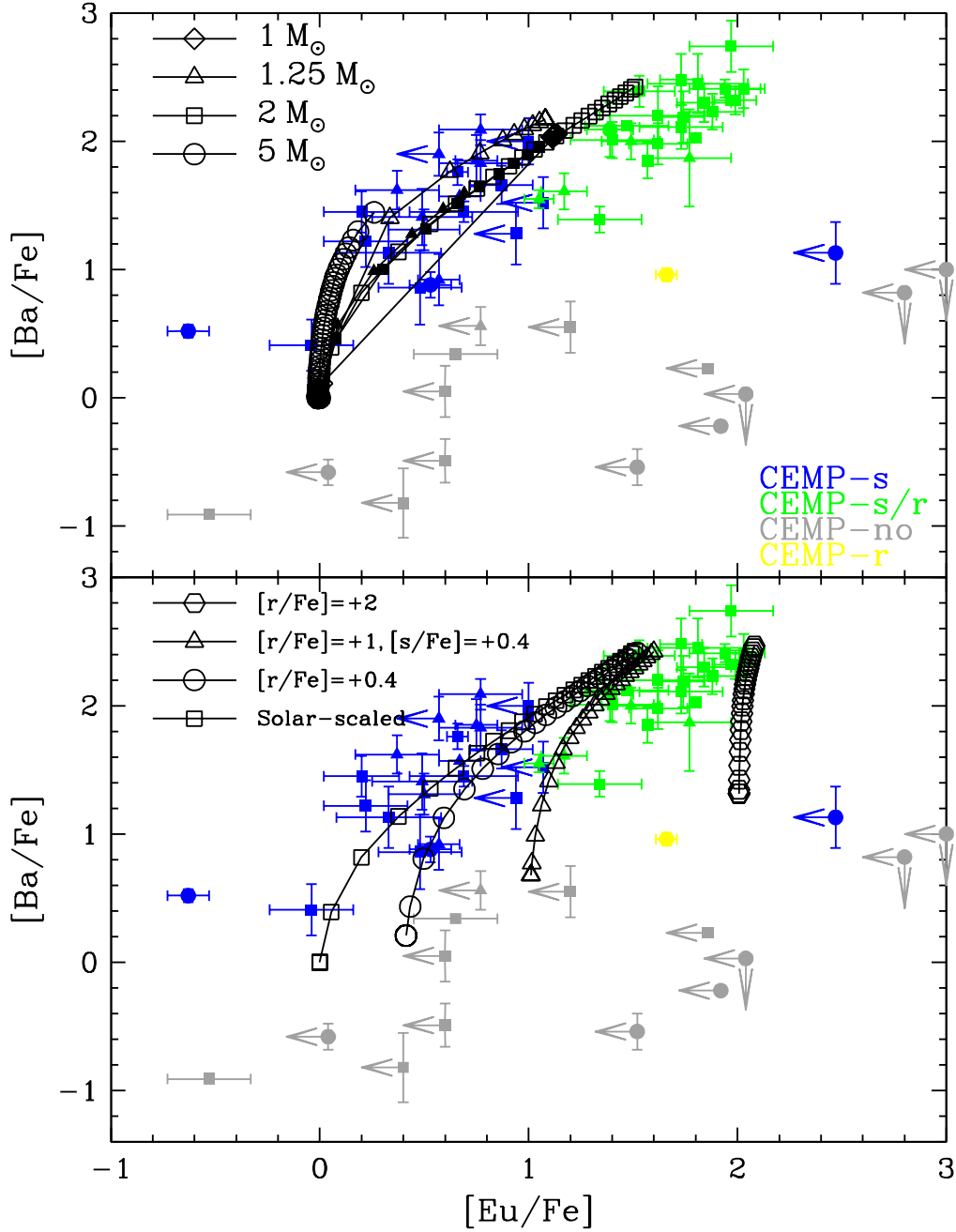


Fig. 6.— A selection of our model predictions is plotted together with the CEMP data of Fig. 5. The predictions lines from our models represent the evolution of the stellar surface composition of the primary AGB stars and each symbol on the lines represents a TP. Top panel: open symbols refer to the Stromlo models and black symbols refer to the STARS models. Stellar masses are indicated in the legend. Bottom panel: open symbols refer to Stromlo models of  $2 M_{\odot}$  and different initial compositions as indicated in the legend. (A color version of this figure is available in the online journal.)

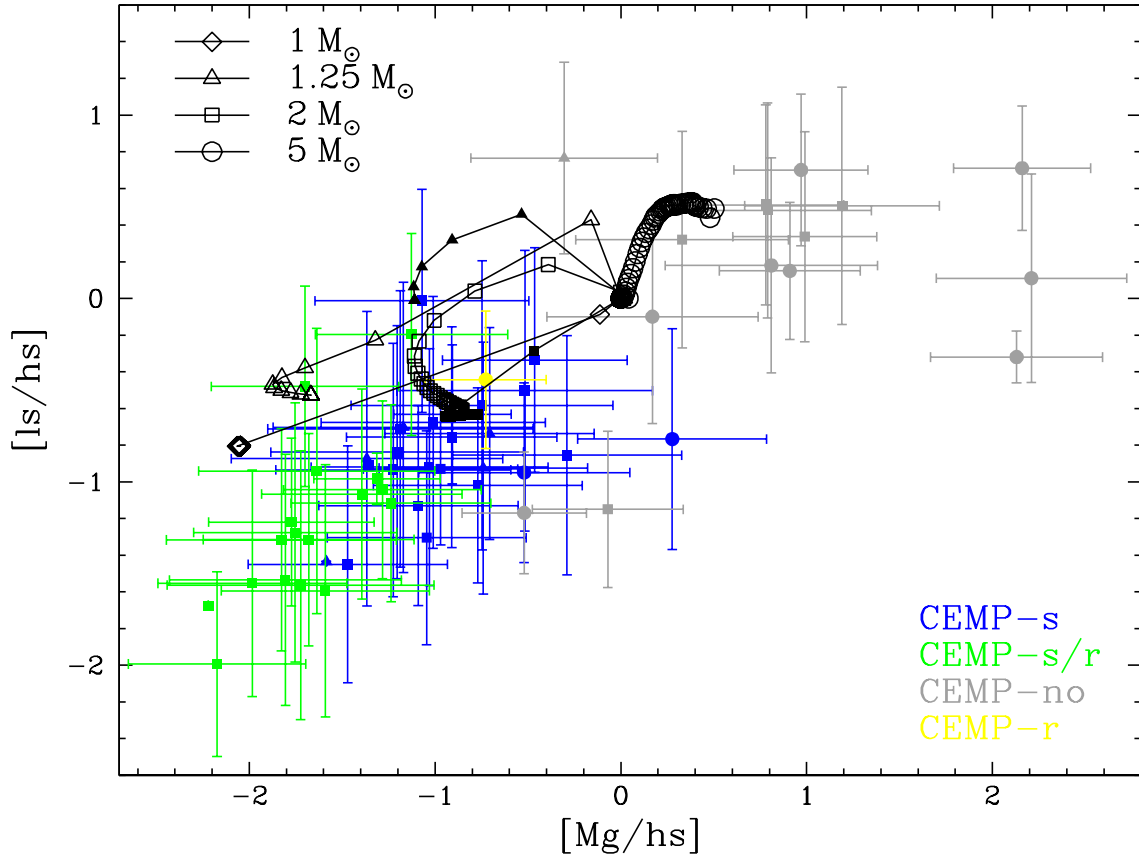


Fig. 7.— Same as Fig. 6 but for  $[ls/hs]$  versus  $[Mg/hs]$ . For data on the ls elements we searched the SAGA database (Suda et al. 2008). (A color version of this figure is available in the online journal.)



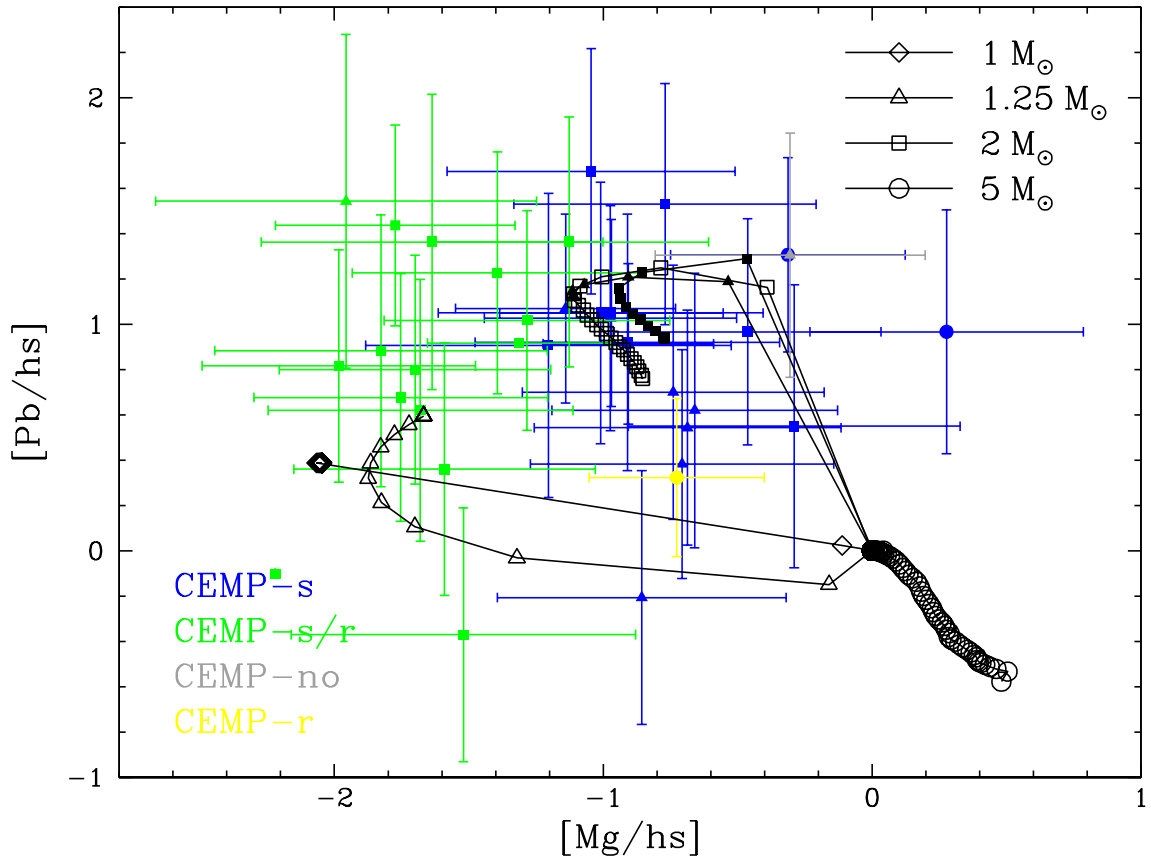


Fig. 8.— Same as Fig. 6 but for [Pb/hs] versus [Mg/hs]. (A color version of this figure is available in the online journal.)

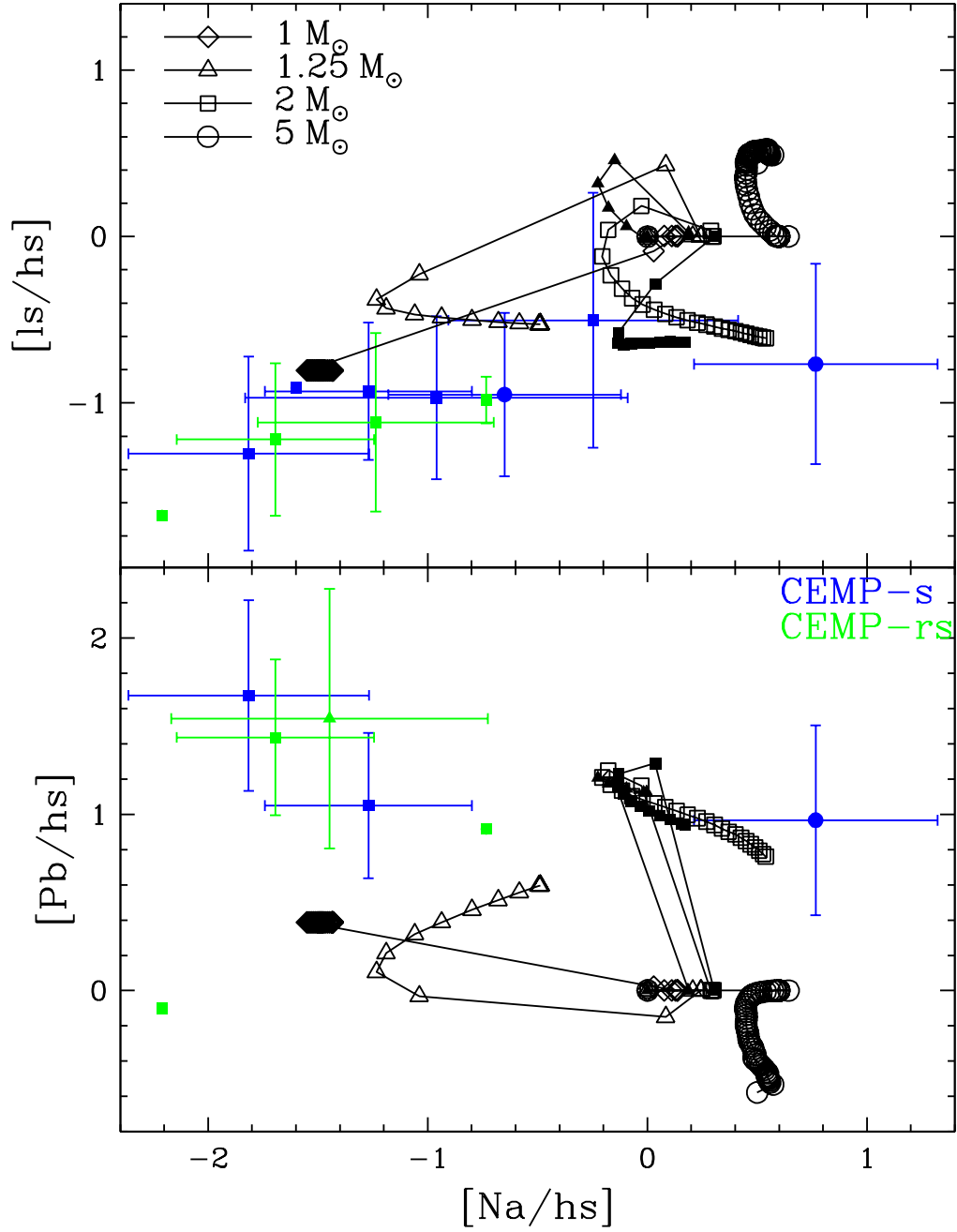


Fig. 9.— Same as Fig. 6 but for  $[ls/hs]$  versus  $[Na/hs]$  (top panel) and  $[Pb/hs]$  versus  $[Na/hs]$  (bottom panel). Data for Na are from Lucatello et al. (2011). (A color version of this figure is available in the online journal.)

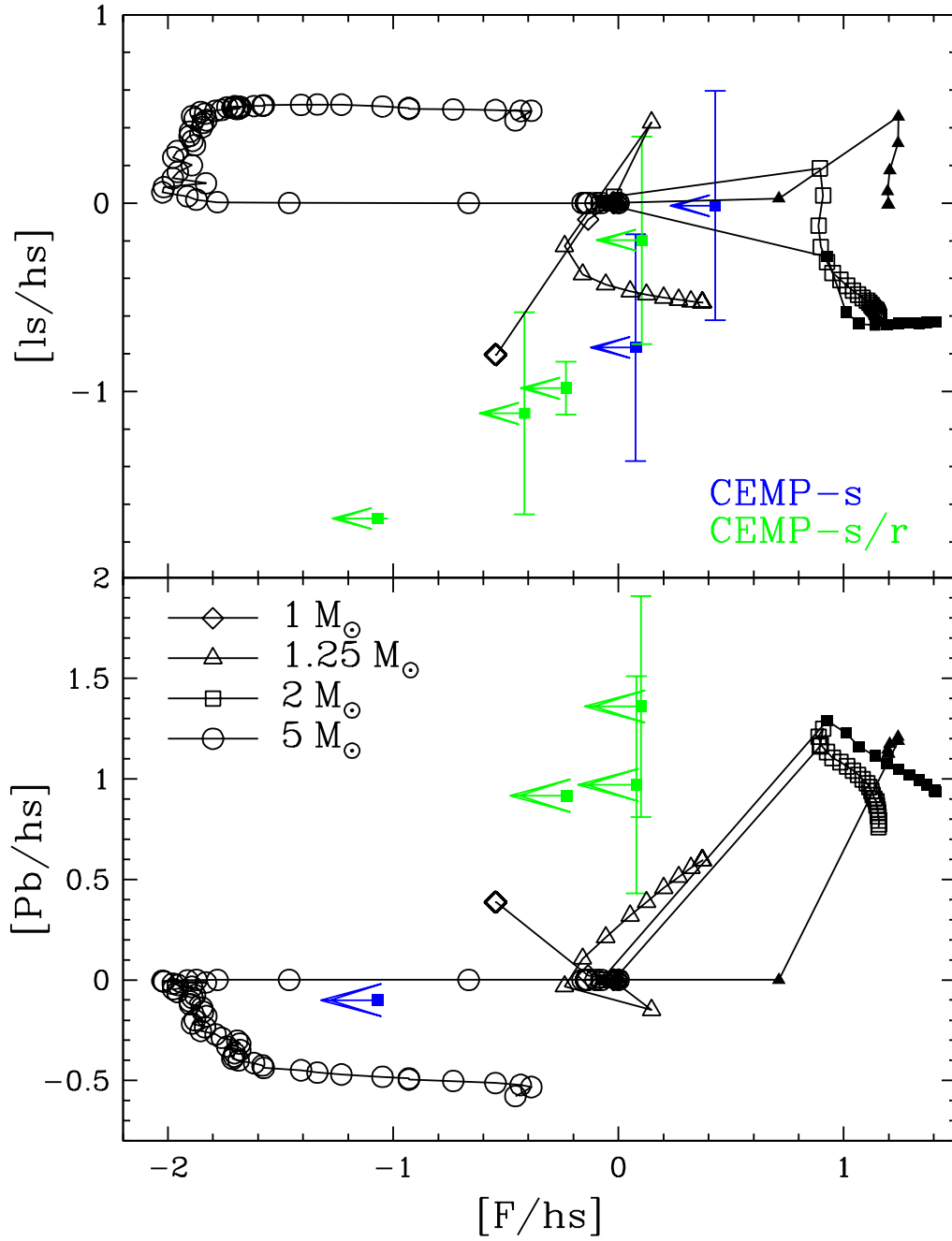


Fig. 10.— Same as Fig. 6 but for  $[ls/hs]$  versus  $[F/hs]$  (top panel) and  $[Pb/hs]$  versus  $[F/hs]$  (bottom panel). Data for F are from Lucatello et al. (2011). (A color version of this figure is available in the online journal.)

Table 1: Details of stellar models computed with the STARS code.

Mass ( $M_{\odot}$ )	TPs	TPs with TDU	$T_{\text{He}}^{\text{max}}$ (MK)	$\lambda_{\text{max}}$	total $M_{\text{dred}}$ ( $M_{\odot}$ )	final $M_{\text{env}}$ ( $M_{\odot}$ )	HBB	$T_{\text{max}}^{\text{bce}}$ (MK)
1.0	13	3-8	273	0.127	0.006	0.016	No	1.64
1.25	9	2-7	267	0.431	0.021	0.015	No	2.75
1.5	9	2-8	268	0.676	0.040	0.408	No	3.97
1.75	11	2-10	276	0.846	0.074	0.08	No	6.05
2.0	13	2-12	283	0.971	0.098	0.468	No	9.79
2.25	13	2-13	294	1.060	0.082	0.584	No	22.04
2.5	16	2-16	298	1.083	0.107	0.789	No	32.05
3.0	16	2-16	331	1.116	0.047	0.979	Yes	56.76

Table 2: Details of stellar models computed with the Stromlo code.

Mass ( $M_{\odot}$ )	TPs	TPs with TDU	$T_{\text{He}}^{\text{max}}$ (MK)	$\lambda_{\text{max}}$	total $M_{\text{dred}}$ ( $M_{\odot}$ )	final $M_{\text{env}}$ ( $M_{\odot}$ )	HBB	$T_{\text{max}}^{\text{bce}}$ (MK)
0.9	38	4-20	278 <sup>a</sup>	0.14	0.012	0.029	No	1.8
1.0	26	5-6	261 <sup>b</sup>	0.18	0.003	0.0085	No	1.5
1.25	16	3-13	274 <sup>c</sup>	0.25	0.020	0.018	No	2.3
1.5	18	3-17	282	0.51	0.059	0.022	No	3.4
1.75	20	3-20	294	0.71	0.132	0.029	No	5.4
1.9	24	3-23	300	0.80	0.169	0.029	No	7.4
2.0	26	2-26	307	0.85	0.218	0.038	No	9.0
	19 <sup>d</sup>	2-18	305	0.85	0.133	0.0 <sup>e</sup>	No	6.6
2.25	33	3-33	320	0.94	0.292	0.162	No	15.7
2.5	30	2-30	351	1.01	0.283	0.413	No	28.4
	21 <sup>d</sup>	1-20	341	0.99	0.165	0.0 <sup>e</sup>	No	16.3
3.0	20	2-20	336	1.02	0.106	0.119	Yes	39.6
3.5	27	2-27	348	1.04	0.103	0.136	Yes	75.9
4.0	37	2-37	352	0.97	0.128	0.133	Yes	82.9
4.5	41	2-41	352	0.96	0.110	0.085	Yes	87.2
5.0	56	2-56	363	0.96	0.106	0.124	Yes	92.5
5.5	77	2-77	369	0.94	0.124	0.085	Yes	98.2
6.0	109	2-109	378	0.93	0.127	0.183	Yes	105

<sup>a</sup>This temperature refers to the TP followed by TDU. The absolute maximum temperature was 302 MK. <sup>b</sup>This temperature refers to the TP followed by TDU. The absolute maximum temperature was 298 MK. <sup>c</sup>This temperature refers to the TP followed by TDU. The absolute maximum temperature was 277 MK. <sup>d</sup>This model was computed using the C and N-rich opacity tables from Lederer & Aringer (2009). <sup>e</sup>This model was evolved to the white dwarf cooling track. The final envelope mass was a few  $10^{-5} M_{\odot}$ , which is the remaining H-shell.

Table 3: Selected key elemental abundances  $[X/Fe]$  at the stellar surface at the end of the computed evolution for all our STARS models with a scaled solar initial composition from Asplund et al (2009).

Mass ( $M_{\odot}$ )	$M_{\text{mix}}$ ( $M_{\odot}$ )	[Na/Fe]	[Mg/Fe]	[Sr/Fe]	[Ba/Fe]	[Eu/Fe]	[Pb/Fe]	[Ba/Sr]	[Ba/Eu]	[Pb/Ba]
1.25	0	0.65	0.08	0.36	0.02	-0.01	0.02	-0.34	0.03	0.00
	0.002	1.62	0.51	1.65	1.59	0.69	2.75	-0.06	0.90	1.16
1.5	0	0.92	0.21	0.07	0.02	-0.01	0.01	-0.05	0.03	-0.01
	0.0006	1.31	0.42	1.46	1.38	0.47	2.49	-0.08	0.91	1.11
	0.002	1.86	0.76	1.64	1.78	0.85	2.91	0.14	0.93	1.13
	0.004	2.28	1.03	1.34	2.03	1.11	3.10	0.69	0.92	1.07
1.75	0	1.58	0.68	0.10	0.04	-0.02	0.02	-0.06	0.12	-0.02
	0.002	2.24	1.15	1.25	1.94	1.03	3.05	0.69	0.91	1.11
2.0	0	1.65	0.92	0.30	0.64	0.08	0.44	0.34	0.56	-0.20
	0.0006	1.90	1.09	0.90	1.52	0.67	2.69	0.62	0.85	1.17
	0.002	2.26	1.32	1.34	2.04	1.12	3.03	0.70	0.92	0.99
	0.004	2.53	1.52	1.59	2.31	1.38	3.12	0.72	0.93	0.81
2.25	0.002	1.86	1.38	1.18	1.85	0.92	2.72	0.67	0.93	0.87
2.5	0.001	1.40	1.24	0.85	1.47	0.60	2.48	0.62	0.87	1.01
	0.002	1.64	1.42	1.06	1.80	0.88	2.59	0.74	0.92	0.79
3.0	0	0.67	0.69	0.47	0.11	0.	0.02	-0.36	0.11	-0.09
	0.0005	1.23	1.19	0.83	1.25	0.42	2.24	0.42	0.83	0.99



Table 4: Selected key elemental abundances  $[X/Fe]$  at the stellar surface at the end of the computed evolution for all our Stromlo models with a scaled solar initial composition from Asplund et al. (2009).

Mass ( $M_{\odot}$ )	$M_{\text{mix}}$ ( $M_{\odot}$ )	[Na/Fe]	[Mg/Fe]	[Sr/Fe]	[Ba/Fe]	[Eu/Fe]	[Pb/Fe]	[Ba/Sr]	[Ba/Eu]	[Pb/Ba]
0.9	0	1.27	0.13	1.55	2.24	1.05	1.85	0.69	1.19	-0.39
	0.002	2.07	0.67	1.56	2.35	1.31	3.02	0.79	1.04	0.67
1.0	0	0.30	0.02	1.14	2.05	1.08	2.29	0.91	0.97	0.24
	0.002	0.64	0.02	1.10	2.03	1.11	2.46	0.93	0.92	0.43
1.25	0	0.60	0.05	1.37	0.76	0.03	0.07	-0.61	0.73	-0.69
	0.002	1.68	0.50	1.51	2.17	1.08	2.76	0.66	1.09	0.59
1.5	0	1.51	0.31	1.57	2.12	0.97	1.80	0.55	1.15	-0.32
	0.0006	1.78	0.55	1.59	2.38	1.37	2.88	0.79	1.01	0.50
	0.002	2.30	0.91	1.64	2.45	1.47	3.15	0.81	0.98	0.70
	0.004	2.68	1.20	1.78	2.51	1.53	3.20	0.73	0.98	0.69
1.75	0	2.30	0.85	1.83	2.27	0.96	1.55	0.44	1.31	-0.72
	0.002	2.75	1.28	1.93	2.54	1.46	3.22	0.61	1.08	0.68
1.9	0.002	2.90	1.45	1.90	2.42	1.45	3.23	0.52	0.97	0.81
2.0	0	2.73	1.35	0.62	0.12	-0.05	0.04	-0.50	0.17	-0.08
	0 <sup>a</sup>	2.09	0.91	0.57	0.16	-0.03	0.03	-0.41	0.19	-0.13
	0.0006	2.81	1.45	1.51	1.89	0.98	2.92	0.38	0.91	1.03
	0.002	3.02	1.62	1.78	2.42	1.51	3.24	0.64	0.91	0.82
	0.002 <sup>a</sup>	2.57	1.30	1.56	2.21	1.30	3.17	0.65	0.91	0.96
2.25	0.004	3.21	1.80	1.98	2.65	1.68	3.28	0.67	0.97	0.63
	0.002	3.07	1.94	1.81	2.51	1.55	3.20	0.70	0.96	0.69
2.5	0.001	2.60	2.05	1.47	2.11	1.18	3.04	0.64	0.93	0.93
	0.002	2.71	2.13	1.72	2.40	1.44	3.14	0.68	0.96	0.74
	0.002 <sup>a</sup>	2.28	1.67	1.50	2.21	1.26	3.04	0.71	0.95	0.83

<sup>a</sup>Model computed with low-temperature opacities from Lederer & Aringer (2009).



Table 4: Continues.

Mass ( $M_{\odot}$ )	$M_{\text{mix}}$ ( $M_{\odot}$ )	[Na/Fe]	[Mg/Fe]	[Sr/Fe]	[Ba/Fe]	[Eu/Fe]	[Pb/Fe]	[Ba/Sr]	[Ba/Eu]	[Pb/Ba]
3.0	0	1.91	1.72	1.40	0.79	0.04	0.19	-0.61	0.75	-0.60
	0.0005	2.08	1.87	1.43	1.76	0.78	2.77	0.33	0.98	1.01
	0.001	2.17	1.92	1.51	2.06	1.08	2.90	0.55	0.98	0.84
3.5	0	1.75	1.59	1.45	1.01	0.09	0.34	-0.44	0.92	-0.67
4.0	0	1.91	1.70	1.58	1.25	0.18	0.50	-0.33	1.07	-0.75
4.5	0	1.75	1.59	1.59	1.34	0.22	0.58	-0.25	1.12	-0.76
5.0	0	1.78	1.74	1.67	1.35	0.20	0.63	-0.32	1.15	-0.72
5.5	0	1.81	1.95	1.84	1.54	0.29	0.82	-0.30	1.25	-0.72
	0.0001	1.80	1.94	1.76	1.60	0.50	2.49	-0.16	1.10	0.89
6.0	0	1.76	1.99	1.93	1.72	0.42	0.96	-0.21	1.30	-0.76

Table 5: Elemental abundances  $[X/Fe]$  for C, N, O, F, and Ne at the stellar surface at the end of the computed evolution for our models with a scaled solar initial composition from Asplund et al. (2009) and  $M_{\text{mix}}=0.002 M_{\odot}$  for  $\text{Mass} < 3 M_{\odot}$  and  $M_{\text{mix}}=0$  for  $\text{Mass} \geq 3 M_{\odot}$ .

Mass ( $M_{\odot}$ )	Stromlo					STARS				
	[C/Fe]	[N/Fe]	[O/Fe]	[F/Fe]	[Ne/Fe]	[C/Fe]	[N/Fe]	[O/Fe]	[F/Fe]	[Ne/Fe]
0.9	2.74	1.82	1.07	2.78	2.06					
1.0	1.86	0.87	0.42	1.52	0.68	2.56	1.37	1.15	2.75	1.88
1.25	2.60	0.98	0.91	2.53	1.84	2.75	1.06	1.22	2.82	1.90
1.5	2.90	1.10	1.17	3.02	2.30	2.84	0.86	1.28	3.04	2.09
1.75	3.10	1.08	1.27	3.40	2.61	2.98	0.83	1.31	3.39	2.35
1.9	3.15	1.14	1.29	3.54	2.72					
2.0 <sup>a</sup>	3.21	1.14	1.31	3.63	2.82	2.78	0.66	1.05	3.27	2.17
2.0 <sup>b</sup>	3.05	1.12	1.17	3.38	2.56					
2.25	3.27	1.06	1.34	3.73	2.93	2.65	0.51	0.92	2.65	2.05
2.5	3.20	0.85	1.30	3.43	2.77	2.60	0.40	0.84	3.10	1.95
2.5 <sup>b</sup>	3.00	0.80	1.11	3.19	2.49					
3.0	3.03	1.46	0.98	2.34	2.00	2.41	1.56	0.65	1.72	0.83
3.5	2.60	3.26	0.95	1.60	1.75					
4.0	2.69	3.43	1.29	2.21	1.95					
4.5	2.55	3.35	1.20	1.80	1.75					
5.0	2.40	3.38	0.91	0.83	1.70					
5.5	2.46	3.42	1.00	0.09	1.67					
6.0	2.28	3.49	1.24	-0.45	1.65					

<sup>a</sup>For comparison, the  $M=2 M_{\odot}$  model by Cristallo et al. (2009b) produces  $[C/Fe]=3.00$ ,  $[N/Fe]=0.86$ ,  $[O/Fe]=1.01$ ,  $[F/Fe]=2.90$ , and  $[Ne/Fe]=2.27$ . <sup>b</sup>Model computed with low-temperature opacities from Lederer & Aringer (2009).

Table 6: Selected key elemental abundances  $[X/Fe]$  at the stellar surface at the end of the computed evolution for different models. (SM) = Stromlo; (S) = STARS models; (B10) = Bisterzo et al. (2010); (C09) = Cristallo et al. (2009b).

Mass ( $M_{\odot}$ )	$M_{\text{mix}}(M_{\odot})$	[Na/Fe]	[Mg/Fe]	[Sr/Fe]	[Ba/Fe]	[Eu/Fe]	[Pb/Fe]	[Ba/Sr]	[Ba/Eu]	[Pb/Ba]
1.25 (SM)	0.002	1.68	0.50	1.51	2.17	1.08	2.76	0.66	1.09	0.59
1.25 (S)	0.002	1.62	0.51	1.65	1.59	0.69	2.75	-0.06	0.90	1.16
1.3 (B10)	$\sim 0.001$ , ST <sup>a</sup>	0.66	0.38	0.32	0.78	0.21	3.22	0.46	0.57	2.44
	$\sim 0.001$ , ST/12	0.48	0.31	0.92	2.05	1.17	2.85	1.13	0.88	0.80
1.5 (SM)	0.0006	1.78	0.55	1.59	2.38	1.37	2.88	0.79	1.01	0.50
	0.002	2.30	0.91	1.64	2.45	1.47	3.15	0.81	0.98	0.70
1.5 (S)	0.0006	1.31	0.42	1.46	1.38	0.47	2.49	-0.08	0.91	1.11
	0.002	1.86	0.76	1.64	1.78	0.85	2.91	0.14	0.93	1.13
1.5 (B10)	$\sim 0.001$ , ST	2.26	1.69	1.34	2.04	1.28	4.06	0.70	0.76	2.02
	$\sim 0.001$ , ST/12	2.27	1.47	2.26	2.73	1.71	3.11	0.47	1.02	0.38
2.0 (SM)	0.0006	2.81	1.45	1.51	1.89	0.98	2.92	0.38	0.91	1.03
	0.002	3.02	1.62	1.78	2.42	1.51	3.24	0.64	0.91	0.82
	0.002 <sup>b</sup>	2.46	1.24	1.72	2.46	1.40	3.16	0.74	1.06	0.70
2.0 (S)	0.0006	1.90	1.09	0.90	1.52	0.67	2.69	0.62	0.85	1.17
	0.002	2.26	1.32	1.34	2.04	1.12	3.03	0.70	0.92	0.99
2.0 (B10)	$\sim 0.001$ , ST	1.89	1.44	1.34	1.87	1.05	4.12	0.53	0.82	2.25
	$\sim 0.001$ , ST/12	1.87	1.19	2.15	2.96	1.98	3.44	0.81	0.98	0.48
2.0 (C09)	$\sim 0.001$ <sup>c</sup>	1.77	1.30	1.01	1.55	0.77	2.88	0.54	0.78	1.33

<sup>a</sup>For the models calculated by Bisterzo et al. (2010) we also need to indicate the choice of the free parameter used in those models to describe the efficiency of the  $^{13}\text{C}$  pocket, where ST corresponds to the standard case, as described in detail by those authors. This free parameter accounts for a possible range of  $^{13}\text{C}$  and  $^{14}\text{N}$  profiles in the  $^{13}\text{C}$  pocket, resulting in a range of total integrated neutron fluxes. Thus, it is the main free parameter determining the final  $s$ -process abundance distribution in these models. <sup>b</sup>Model computed with the opacities by Lederer & Aringer (2009). <sup>c</sup>In the models calculated by Cristallo et al. (2009b) the  $^{13}\text{C}$  pocket is included self-consistently using an overshooting mechanism with the free parameter  $\beta=0.1$ , as described in details in that paper. This results in a mixing mass of the order of  $\sim 0.001 M_{\odot}$ , but decreasing with the TP number, while in our models it is kept constant. Furthermore, the resulting proton profile is not linear in logarithmic scale (see Fig. 4 of Cristallo et al. 2009b), as imposed in our models.